

X-RAY PROPERTIES OF LINERS AND LOW-LUMINOSITY SEYFERT GALAXIES OBSERVED WITH ASCA. I. OBSERVATIONS AND RESULTS

YUICHI TERASHIMA^{1,2}, NAOKO IYOMOTO¹, LUIS C. HO³, AND ANDREW F. PTAK^{4,5}
To appear in The Astrophysical Journal Supplement series.

ABSTRACT

This paper presents a comprehensive study of the X-ray properties of low-ionization nuclear emission-line regions (LINERs) and low-luminosity Seyfert galaxies based on observations obtained with the ASCA satellite. We analyzed data of 53 observations of 21 LINERs and 17 low-luminosity Seyferts. X-ray emission has been detected in all but one object. The X-ray luminosities in the 2–10 keV band range from 4×10^{39} ergs s⁻¹ to 5×10^{41} ergs s⁻¹, which are 1–3 orders of magnitude smaller than in classical Seyfert galaxies. The X-ray spectra of most objects are well described by a canonical model which consists of (1) a soft component from a thermal plasma with $kT < 1$ keV and (2) a hard component represented by a power law with a photon index of $\Gamma \approx 1.8$ or thermal bremsstrahlung emission with $kT \approx 10$ keV. Several objects do not require the soft thermal component, and their continua are well fitted by a single power-law model. Some objects show heavy absorption with column densities in excess of 10^{23} cm⁻². We detect in several objects Fe K line emission with equivalent widths ranging from 50 eV to 2 keV.

Variability on timescales less than a day is uncommon in our sample. By comparing multiple observations made with ASCA or with published 2–10 keV observations from other satellites, we show that at least eight objects are variable on timescales of a week to several years. We find that the morphologies of many objects, both in the soft and hard bands, are consistent with being pointlike relative to the telescope point-spread function; a few are clearly extended in either or both energy bands.

The second paper of this series will discuss the physical interpretation of the X-ray emission and its implications for low-luminosity active galactic nuclei.

Subject headings: galaxies: active — galaxies: nuclei — galaxies: Seyfert — X-rays: galaxies

1. INTRODUCTION

It is widely accepted that many bright galaxies possess low-level nuclear activity. The Palomar optical spectroscopic survey of nearby galaxies by Ho, Filippenko, & Sargent (1995, 1997a, 1997b) showed that more than 40% of the 486 galaxies with $B_T \leq 12.5$ mag and $\delta > 0^\circ$ have optical spectra classified as Seyfert nuclei, low-ionization nuclear emission-line regions (LINERs; Heckman 1980), or transition objects (spectra intermediate between LINERs and H II nuclei)⁶. It is not clear, however, what fraction of these objects are genuine active galactic nuclei (AGNs), which we take to be objects powered by non-stellar processes. Extensive observations have been made in various wavelengths to clarify the nature of these classes of objects (for reviews see Ho 1999, 2002). X-ray observations play a key role in this regard. This paper presents the first systematic analysis of a large sample of LINERs and low-luminosity Seyfert galaxies observed with the ASCA satellite.

The gross spectroscopic characteristics of LINERs can be explained by a variety of ionization mechanisms, including traditional photoionization by a low-luminosity AGN (LLAGN), photoionization by a population of unusually hot stars, and mechanical heating by shock waves. Recent reviews on this topic have been given by Filippenko (1996) and Barth (2002). If LINERs are low-luminosity versions of AGNs, which are powered by accretion onto massive black holes, we expect them to emit

nonthermal, hard X-rays. On the other hand, X-rays from thermal plasmas are expected from shock-heated gas. Hot stars also have soft thermal spectra in the X-ray band. Thus, X-ray observations can help discriminate between the various models for LINERs. We note, however, that hard X-rays (hereinafter defined as $E > 2$ keV) are not a signature unique to AGNs: potential contributors to the hard-energy band include X-ray binaries, supernovae, and hot ($kT \approx 10$ keV) gas produced by starburst activity. An unambiguous search for AGNs using X-ray data thus requires careful consideration of the spectral, structural, and variability properties of the sources.

Many Seyfert galaxies have been identified in the Palomar survey. The median H α luminosity of these sources is $L_{H\alpha} \approx 2 \times 10^{39}$ ergs s⁻¹, which is more than 2–3 orders of magnitude lower than in classical Seyfert galaxies (e.g., Dahari & De Robertis 1988; Whittle 1992). X-ray observations of such low-luminosity Seyferts (hereinafter LLSeyferts) are necessary to determine whether they are genuine AGNs and whether they are similar to luminous AGNs.

In addition to studying the origin of activity in LINERs and LLSeyferts, the X-ray properties of these sources themselves hold great interest. By defining an LLAGN sample using strong AGN candidates based on detailed study of individual objects, we can investigate the nature of LLAGNs as a class, compare them with more luminous AGNs, and potentially constrain

¹ Institute of Space and Astronautical Science, 3-1-1 Yoshinodai, Sagami-hara, Kanagawa 229-8510, Japan.

² Astronomy Department, University of Maryland, College Park, MD 20742.

³ The Observatories of the Carnegie Institution of Washington, 813 Santa Barbara St., Pasadena, CA 91101-1292..

⁴ Department of Physics, Carnegie Mellon University, 5000 Forbes Ave., Pittsburgh, PA 15213.

⁵ Department of Physics and Astronomy, Johns Hopkins University, 3400 North Charles St., Baltimore, MD 21218-2686.

⁶ In this paper, we use the classifications based on optical emission-line ratios given by Ho et al. (1997a).

models for accretion flows. For example, the spectral properties (continuum shape, absorption column, Fe K-line strength, presence or absence of ionized absorbers) and variability characteristics can be used to probe the structure of the central engine, in a region of parameter space that is likely to be quite unique because of the extreme conditions involved. In the regime of low mass accretion rate, it has been suggested that advection-dominated accretion flows may be present (Narayan & Yi 1994; see reviews by Kato, Fukue, & Mineshige 1998 and Quataert 2001). Comparisons between observations and theoretical predictions are critical for testing these and other ideas.

X-ray observations of LINERs and LLSeyferts, both in the soft and hard energy bands, have been published by a number of authors. However, most, if not all, previous studies have been limited either by sample size or restricted energy bandwidth. In the soft X-ray band, data based on observations with *Einstein* and *ROSAT* have been presented by Halpern & Steiner (1983), Koratkar et al. (1995), Komossa, Böhringer, & Huchra (1999), Roberts & Warwick (2000), Lira, Lawrence, & Johnson (2000), and Halderson et al. (2001). The primary disadvantages of observations in the soft X-ray band are contamination by emission from hot gas, often observed in galaxies, and decreased sensitivity to absorbed AGNs. The number of hard X-ray observations of LINERs and LLSeyferts prior to *ASCA* is very limited. Because of sensitivity limitations, only a few of the brightest objects have been observed (e.g., M81 and NGC 3998). The significantly improved sensitivity and imaging capability in the broad energy band (0.5–10 keV) of *ASCA* provide an unprecedented opportunity to study systematically objects with low-level activity.

This paper presents a comprehensive analysis of *ASCA* observations of LINERs and LLSeyferts. In a subsequent paper (Terashima et al. 2001, hereinafter Paper II), we discuss the origin of the X-ray emission using the X-ray properties derived here, along with comparisons with data from other wavelengths, and the broader implications for LLAGNs. Previous *ASCA* results based on smaller samples can be found in Serlemitsos, Ptak, & Yaqoob (1996), Terashima (1998, 1999a, 1999b), Awaki (1999), and Ptak et al. (1999). The references for *ASCA* results on individual objects are given in Terashima, Ho, & Ptak (2000a) and section 9 in this paper. This paper is organized as follows. We define the sample in section 2. Section 3 briefly presents the observations and data reduction. The results of a spectral analysis, a summary of the best-fit spectral parameters, and a tabulation of the derived fluxes and luminosities are presented in sections 4, 5, and 6, respectively. Sections 7 and 8 are devoted to timing and imaging analyses, respectively. Notes on individual objects are given in section 9. Section 10 summarizes the main results.

2. THE SAMPLE

The galaxies in this study were chosen from the Palomar survey of nearby galaxies. We selected objects classified by Ho et al. (1997a) as LINERs and Seyfert galaxies which were either in the *ASCA* data archives as of 1999 December or belonged to our own proprietary observing programs. We decided to analyze Seyferts with $L_{\text{H}\alpha} < 10^{41}$ ergs s⁻¹, roughly the luminosity of NGC 4051, the lowest luminosity “classical” Seyfert galaxy. Luminous Seyferts which have been extensively studied were excluded. The list of galaxies we analyzed is shown in Table

1, where we list the Hubble types, distances, heliocentric velocities, and optical spectroscopic classifications. We use the distances adopted by Ho et al. (1997a), which are taken from Tully (1988) and are based on a Hubble constant of $H_0 = 75$ km s⁻¹ Mpc⁻¹. The velocities are taken from the NASA/IPAC Extragalactic Database (NED).

We omitted a few objects with ambiguous spectral classification. The LINER 2 NGC 4486 (M87) was also excluded because of the complexity of its X-ray emission (Matsumoto et al. 1996; Reynolds et al. 1996; Allen, Di Matteo, & Fabian 2000). The X-ray spectrum of M87 consists of multiple components, namely emission from an AGN and hot gas from the host galaxy and the Virgo cluster. Properly measuring the spectral parameters of the AGN component requires detailed image analysis and a sophisticated modeling of the thermal emission, including the effects of multiple temperatures, metal abundances, and temperature and metallicity gradients. This is beyond the scope of this paper.

The two transition objects NGC 4569 and NGC 4192, which were analyzed by Terashima et al. (2000b), were included. Several objects in the southern hemisphere (NGC 1097, 1365, 1386, and 4941), which have good *ASCA* data, were also used. The optical classifications for these objects were taken from Phillips et al. (1984), Storchi-Bergmann, Baldwin, & Wilson (1993), Véron-Cetty & Véron (1986), and Storchi-Bergmann & Pastoriza (1989).

The final sample consists of nine LINER 1s, 12 LINER 2s, eight Seyfert 1s, and nine Seyfert 2s. Some of these objects were observed at least twice with *ASCA*. Whenever possible we analyzed the multiple observations to achieve better photon statistics and to search for variability. In total there are 53 observations, as summarized in Table 2. Section 9 gives comments on the observations which were not used.

3. OBSERVATIONS AND DATA REDUCTION

A log of the *ASCA* observations is shown in Table 2. It gives the start date of the observations, observation modes, count rates obtained for the SIS and GIS detectors, and net exposure times after data screening. The GIS detectors (Ohashi et al. 1996; Makishima et al. 1996) were operated in the PH mode with the nominal bit assignment for all the observations. The spread discriminator was not turned on in the observations of NGC 3079, 4258, and 5194. The clocking and telemetry modes of the SIS detectors (Burke et al. 1994; Yamashita et al. 1999) are also summarized in Table 2. In the SIS observations, in which both the faint and bright modes were used, the two data sets were combined after the faint-mode data were converted to the format of the bright-mode data; the only exception was the 1995 observation of NGC 4579 (see Terashima et al. 1998a).

The data were screened using the following set of criteria: (1) elevation angle above the Earth’s limb greater than 5°, (2) cut-off rigidity greater than 6 GeV c⁻¹, (3) avoidance of South Atlantic Anomaly, and (4) elevation angle above the day Earth’s limb greater than 25° (SIS only). X-ray spectra and light curves were extracted from a circular region with a typical radius of 3’–4’ for SIS and 6’ for GIS. A smaller extraction radius was used in some cases to avoid a bright nearby source. Background spectra were accumulated from a source-free region in the same field.

4. SPECTRAL ANALYSIS

We fitted the SIS and GIS spectra simultaneously using the XSPEC spectral-fitting package (version 10). The spectra of the two SIS detectors were combined, as were those from the two GIS detectors. The quoted errors are at the 90% confidence level for one interesting parameter ($\Delta\chi^2 = 2.7$). The Galactic absorption column densities are derived from HI measurements by Murphy et al. (1996), when available, or else from those by Dickey & Lockman (1990). The results of the spectral fits are presented in Figures 1a–1l. In each figure, the left column displays the SIS spectra, the right column the GIS spectra. Within each plot, the upper panel shows the data and the best-fit model, and the lower panel shows the residuals of the fit. For multi-component models, we plot each component with a different line type in the upper panel.

4.1. Simple Models

We fitted the spectra with a simple power-law model modified by photoelectric absorption along the line of sight. We added a Gaussian component to those objects which showed an indication of a linelike emission feature around 6 keV. The results of the fits are shown in Table 3. Errors are not shown for the fits with poor reduced χ^2 because the error estimations using the $\Delta\chi^2 = 2.7$ criterion are not valid. Acceptable fits were obtained for only several objects: NGC 3031, 3147, 3507, 3998, 4203, 4579 (1998 observation), 4639, and 5033. The other objects show significant residuals in the soft-energy band and/or a more complicated continuum shape. In many objects emission lines are seen in the region 0.6–2 keV, indicative of the presence of a sub-keV thermal plasma. In the next subsection we evaluate a model consisting of a hard component and a soft thermal plasma component.

Several objects show both a heavily absorbed hard component and a less absorbed soft component. In order to fit such a spectral shape, we tried a partially covered power-law model. This model is equivalent to one consisting of a combination of an absorbed power law plus and a scattered power law, as is often observed in Seyfert 2 galaxies (e.g., Turner et al. 1997; Awaki et al. 2000) if one assumes that the power-law slopes of these two components are same. Although the power-law slopes of the soft and hard components could be different, we assumed that they have the same slope because of limited photon statistics. We considered this model for NGC 1052, 2273, 2639, 2655, 4565, and 4941; the results are shown in Table 4. Some of these objects (NGC 1052, 2639, 2655, and 4565) seem to have a softer component accompanied by emission lines from a thermal plasma. In the next subsection, we examine a multi-component model which consists of a partially covered power law and a soft thermal plasma.

We also tried a thermal bremsstrahlung model instead of a power-law model. Again, we added a Gaussian line when a linelike feature was seen around 6 keV. We did not attempt the thermal bremsstrahlung model for those objects with a heavily absorbed continuum shape, since the temperature cannot be well determined and a heavily absorbed continuum is likely to indicate the presence of an obscured AGN. The result of these fits are given in Table 5. Again errors are not shown for the fits with poor reduced χ^2 . This thermal model resulted in significantly worse fits for those objects which were well fitted with a power-law (plus Gaussian) model, except for the relatively faint objects NGC 3507 and NGC 4639, for which χ^2 values similar to those of the power-law fits were obtained. Note that these

two galaxies are fainter than the rest of objects which are well fitted with a simple power-law model.

4.2. Two-component Models

Only a few objects were represented successfully by a simple power-law model; the majority indicated the presence of emission from a soft thermal plasma in addition to the hard component. Therefore, we investigated multiple-component models. We first adopted a model consisting of an absorbed power law plus a Raymond-Smith (RS; Raymond & Smith 1977) thermal plasma modified by Galactic absorption. The abundance was allowed to vary only if a meaningful constraint could be obtained. In many cases the abundance was not well constrained and was fixed at 0.1 solar or 0.5 solar, values typically observed for thermal plasmas in normal and starburst galaxies. A Gaussian line was also added if a linelike feature was seen around 6 keV. When the continuum shape suggests the presence of both a heavily absorbed and a lightly absorbed component, we used a partially covered power-law model instead of a simple power law; this applied to NGC 1052, 2655, and 4565. Both models were tried for NGC 2639. The results of the fits are summarized in Table 6. The fits were successful for all the objects except NGC 4258 (1993 observation) and NGC 4636, which show very complicated spectra.

Thus, a model consisting of an RS plasma plus a hard power-law component can be applied to nearly all objects, with a few objects not requiring the soft component. This “canonical” model successfully represents the spectra of the LINERs and LLSeyferts discussed here. Ptak et al. (1999) found that this model was also applicable to starburst galaxies.

In objects whose continuum was not heavily absorbed, we also evaluated the possibility that in the two-component model the power law could be substituted by a thermal bremsstrahlung model. In all the cases, we obtained χ^2 values (Table 7) similar to those for the RS plasma plus power-law model.

Some objects show apparently weak Fe L emission compared to other emission lines such as the K lines from O, Ne, Mg, and Si. For these objects, we fitted the abundances of Fe and the α -processed elements separately. We fixed the abundances of the α -processed elements at 0.5 solar because the photon statistics are too limited to allow these abundances to be constrained individually. The abundance of Fe was allowed to vary. We assumed a power-law shape for the hard component in these fits. Only objects with a relatively good signal-to-noise ratio for the soft component were fitted with this model. The results are tabulated in Table 8. The χ^2 values show improvement for NGC 1097, 3079, 4636, and 5194, compared to the case of a RS plasma with solar abundance ratios.

4.3. Complex Models

The spectra of only two objects, NGC 4258 (1993 observation) and NGC 4636, cannot be fitted with the models described above. As discussed in section 9, we applied more complex models to these objects.

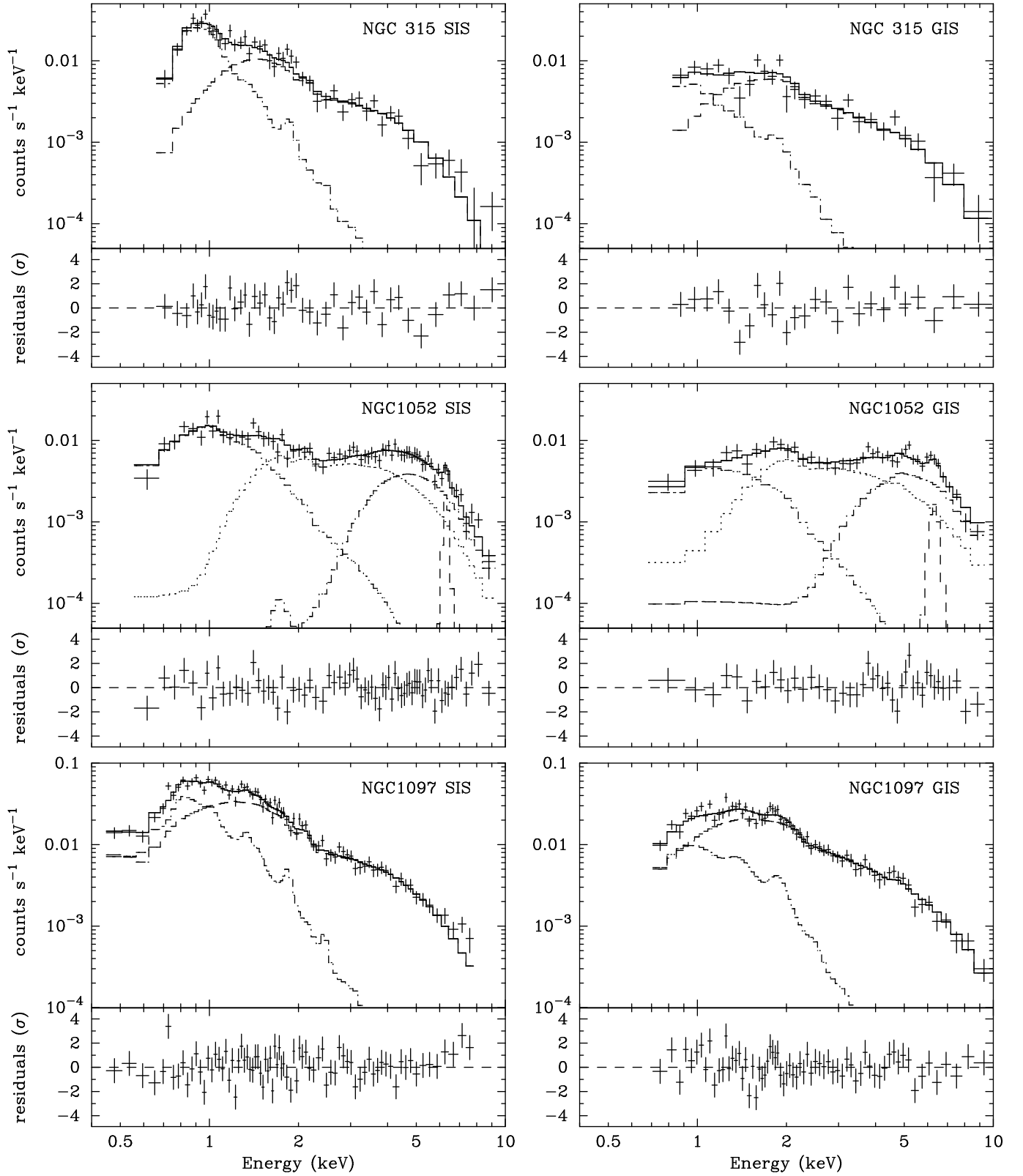


FIG. 1a.— ASCA SIS (left) and GIS (right) spectra. In each plot, the upper panel shows the data and the model, and the lower panel shows the residuals of the fit. (a) NGC 315 (top), NGC 1052 (middle), NGC 1097 (bottom).

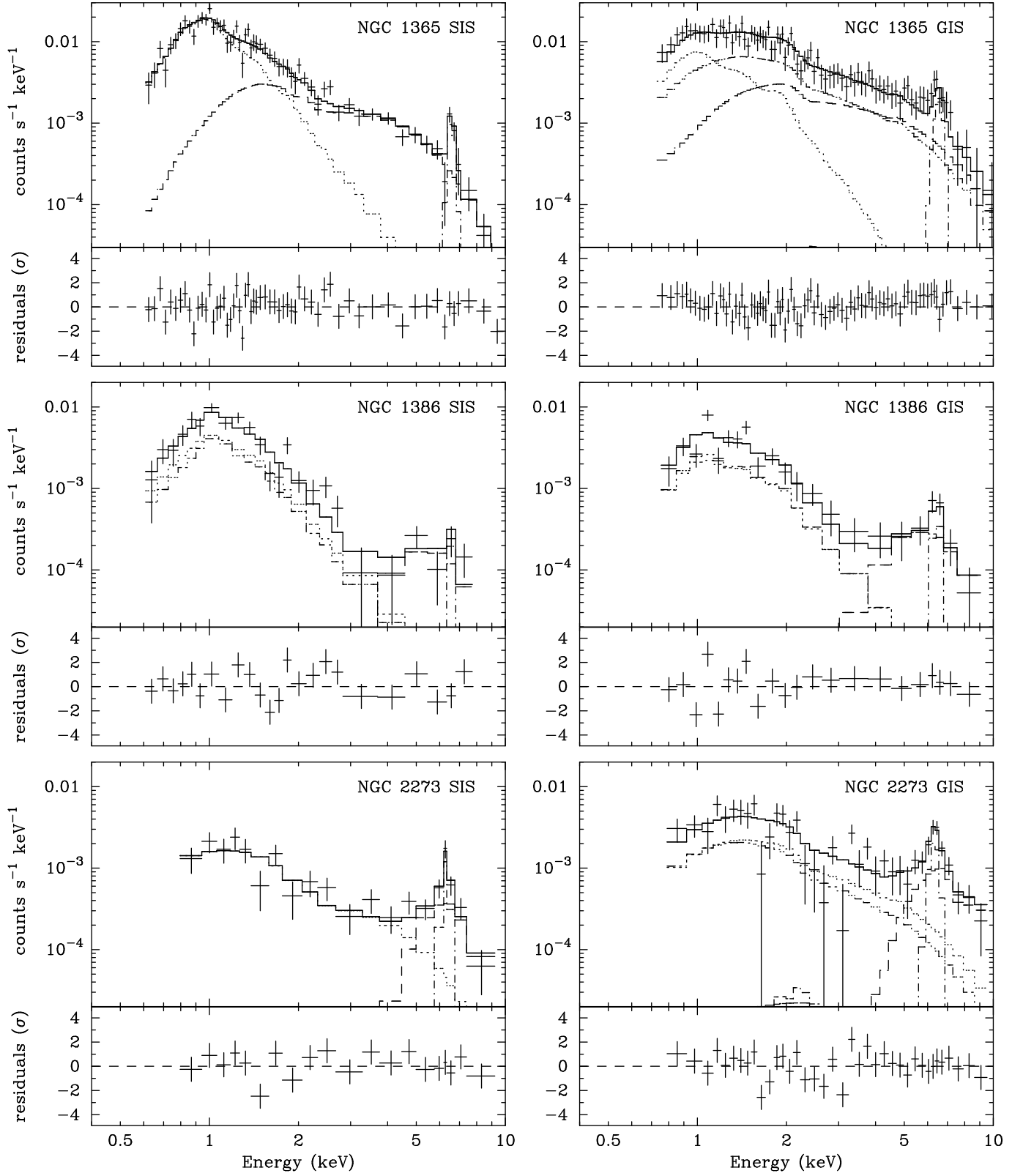


FIG. 1b.— Same as in Figure 1a. (b) NGC 1365 (top), NGC 1386 (middle), NGC 2273 (bottom).

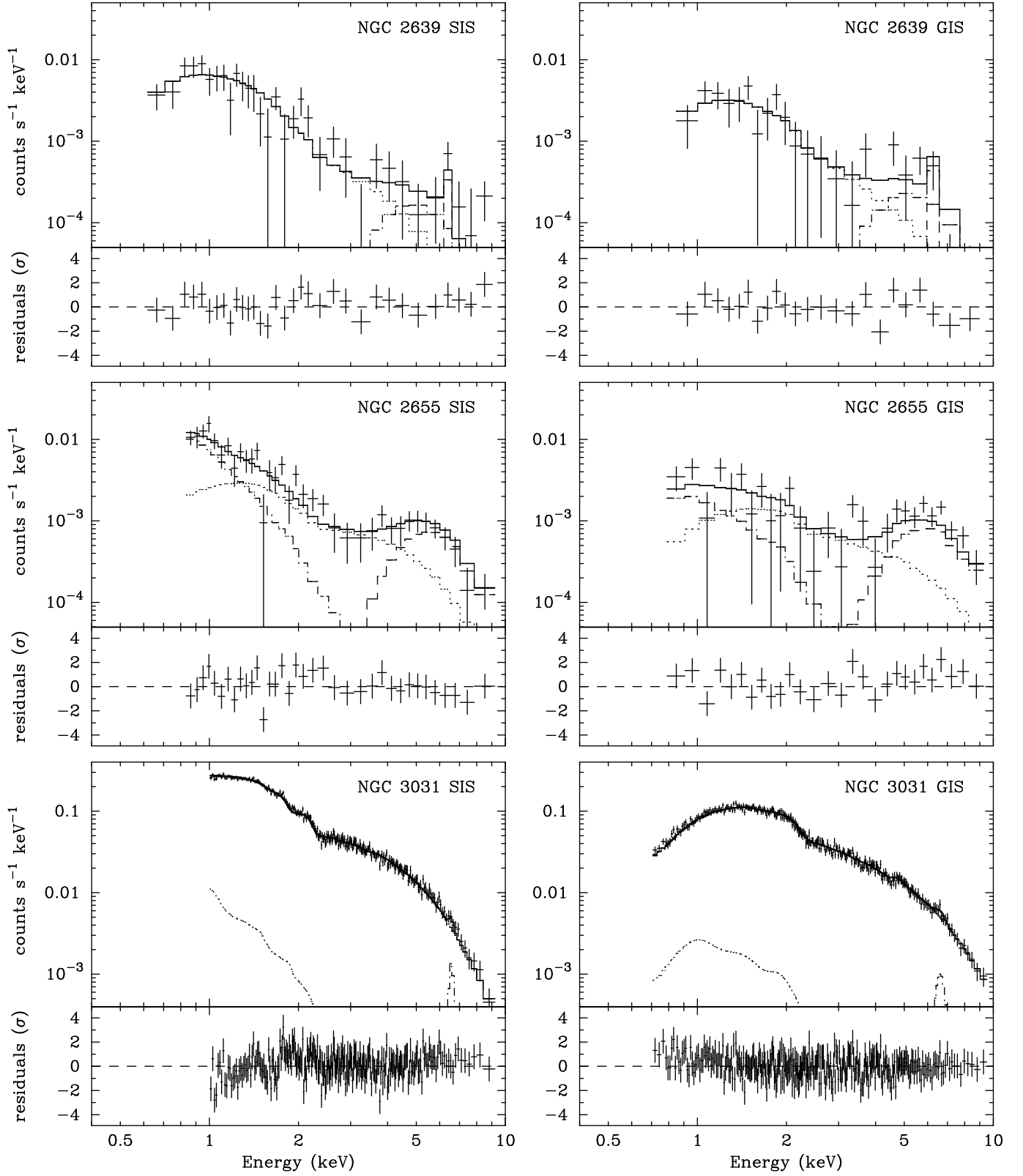


FIG. 1c.— Same as in Figure 1a. (c) NGC 2639 (top), NGC 2655 (middle), NGC 3031 (bottom).

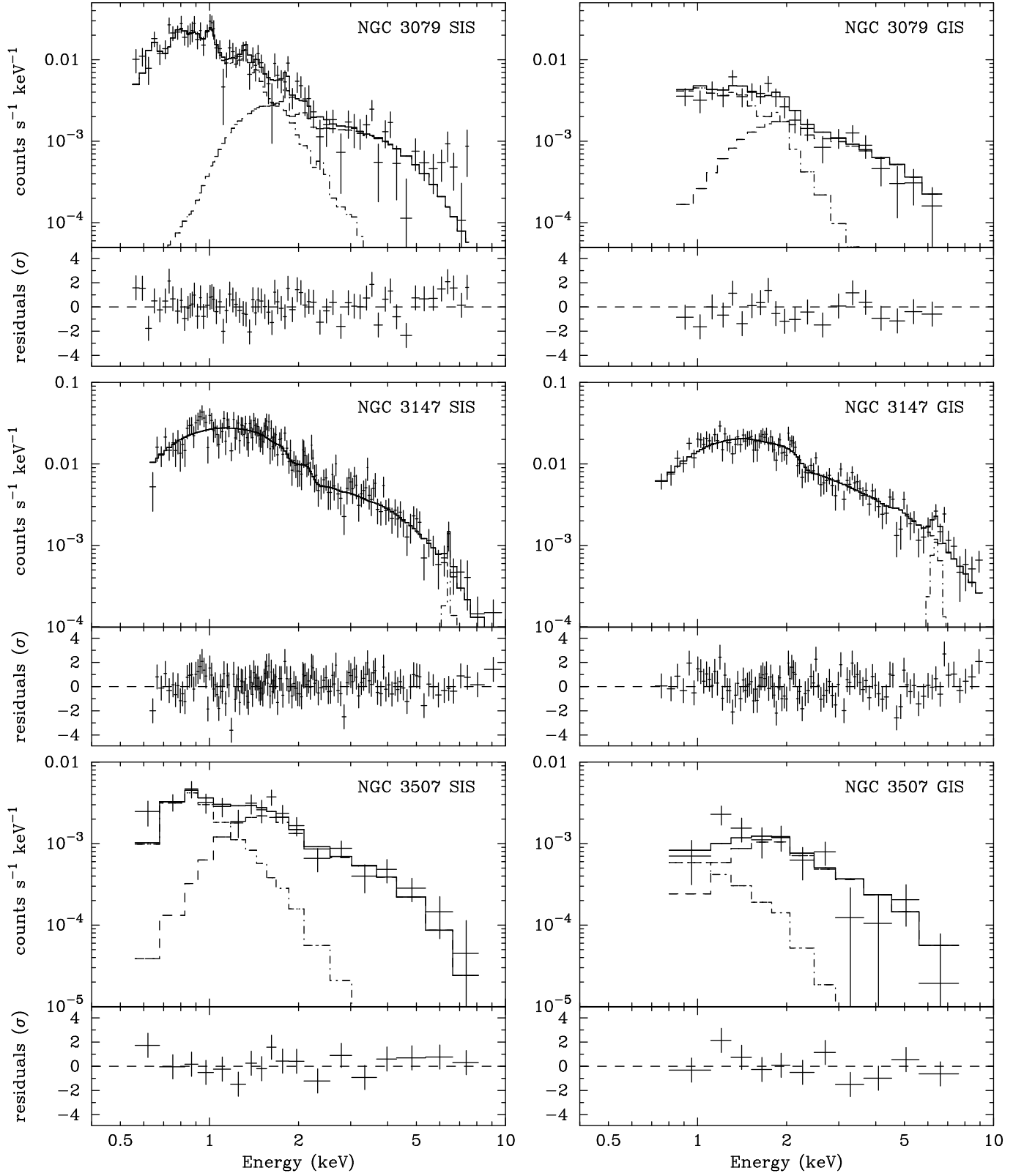


FIG. 1d.— Same as in Figure 1a. (d) NGC 3079 (top), NGC 3147 (middle), NGC 3507 (bottom).

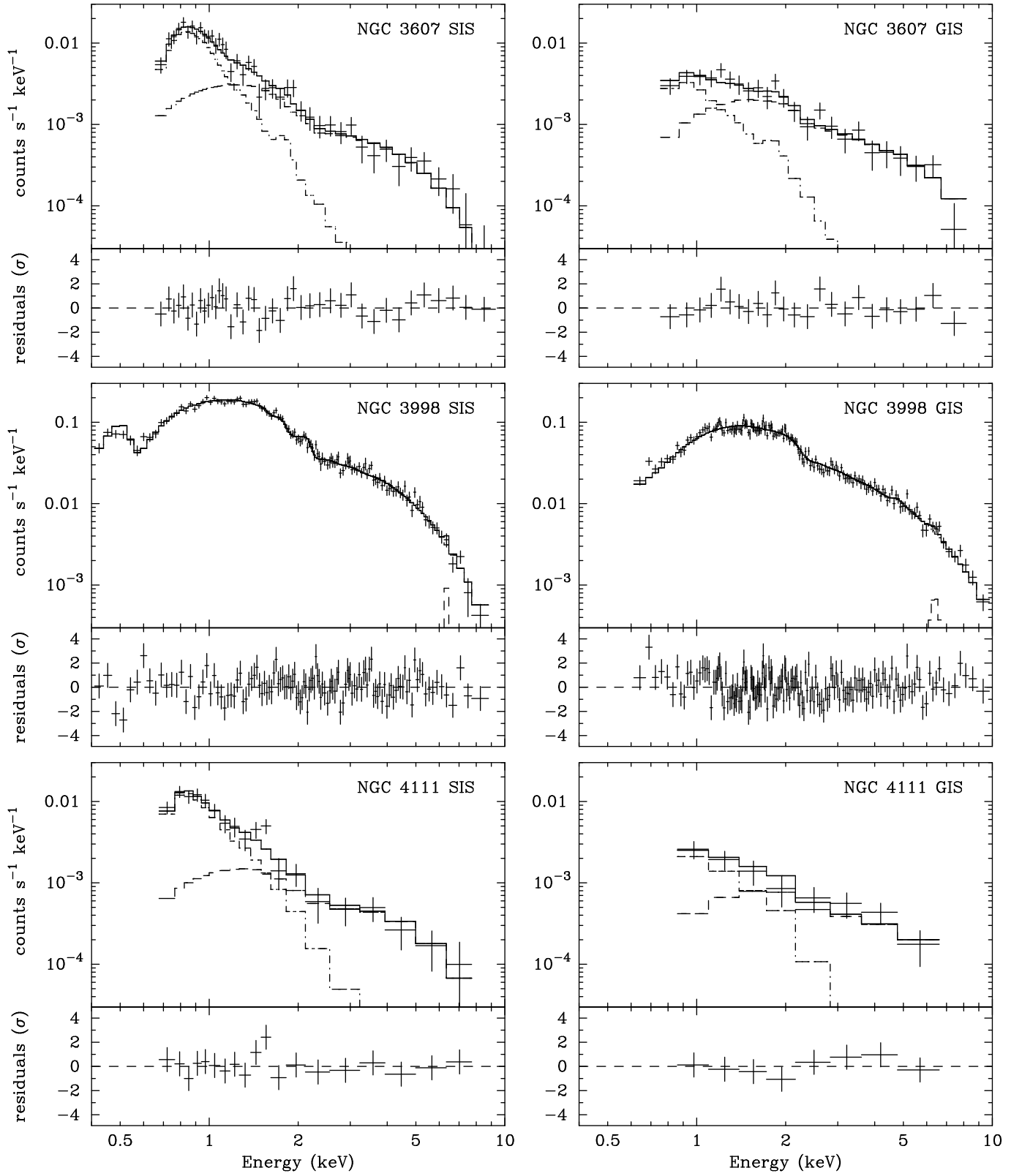


FIG. 1e.— Same as in Figure 1a. (e) NGC 3607 (top), NGC 3998 (middle), NGC 4111 (bottom).

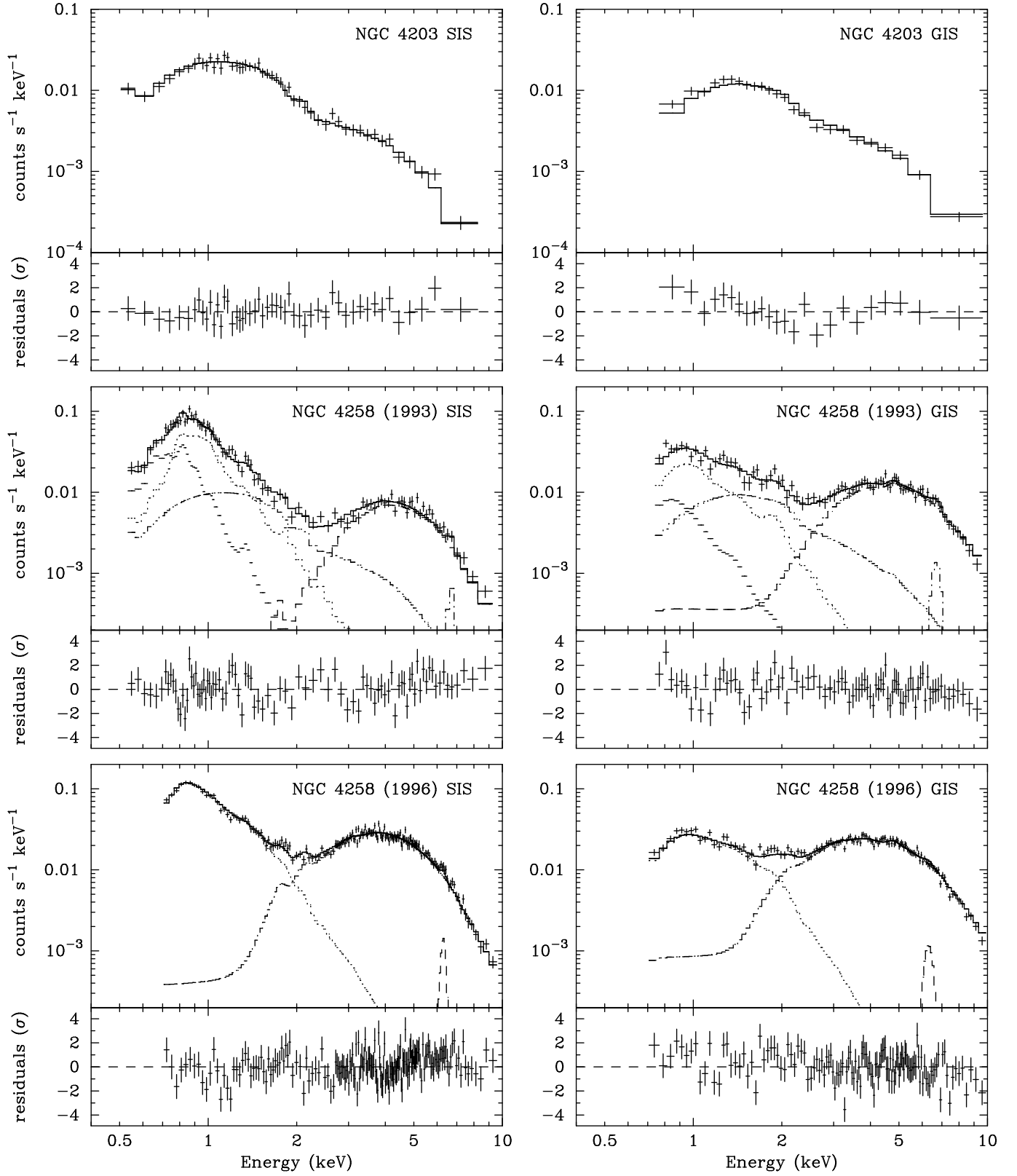


FIG. 1f.— Same as in Figure 1a. (f) NGC 4203 (top), NGC 4258 (1993) (middle), NGC 4258 (1996) (bottom).

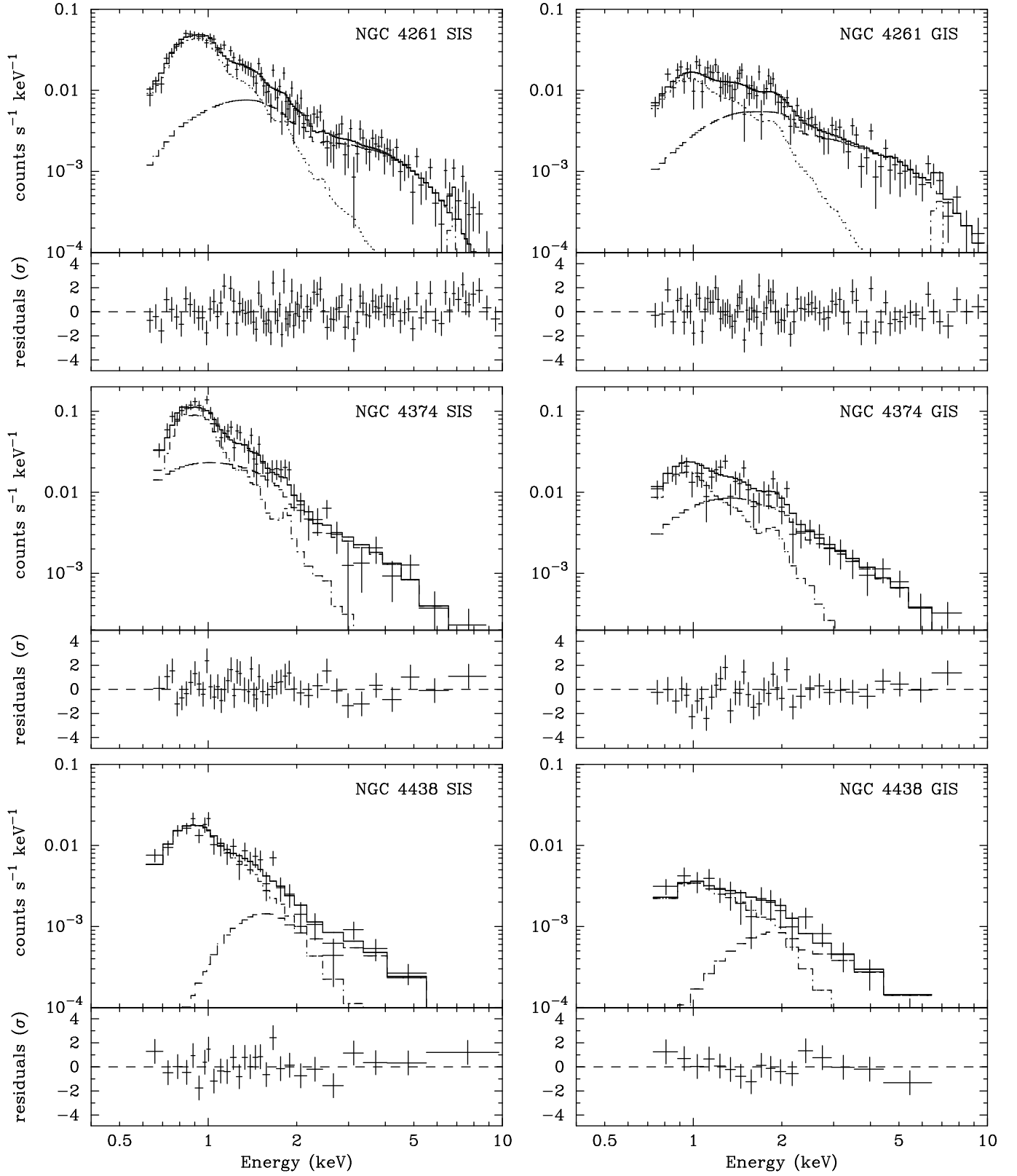


FIG. 1g.— Same as in Figure 1a. (g) NGC 4261 (top), NGC 4374 (middle), NGC 4438 (bottom).

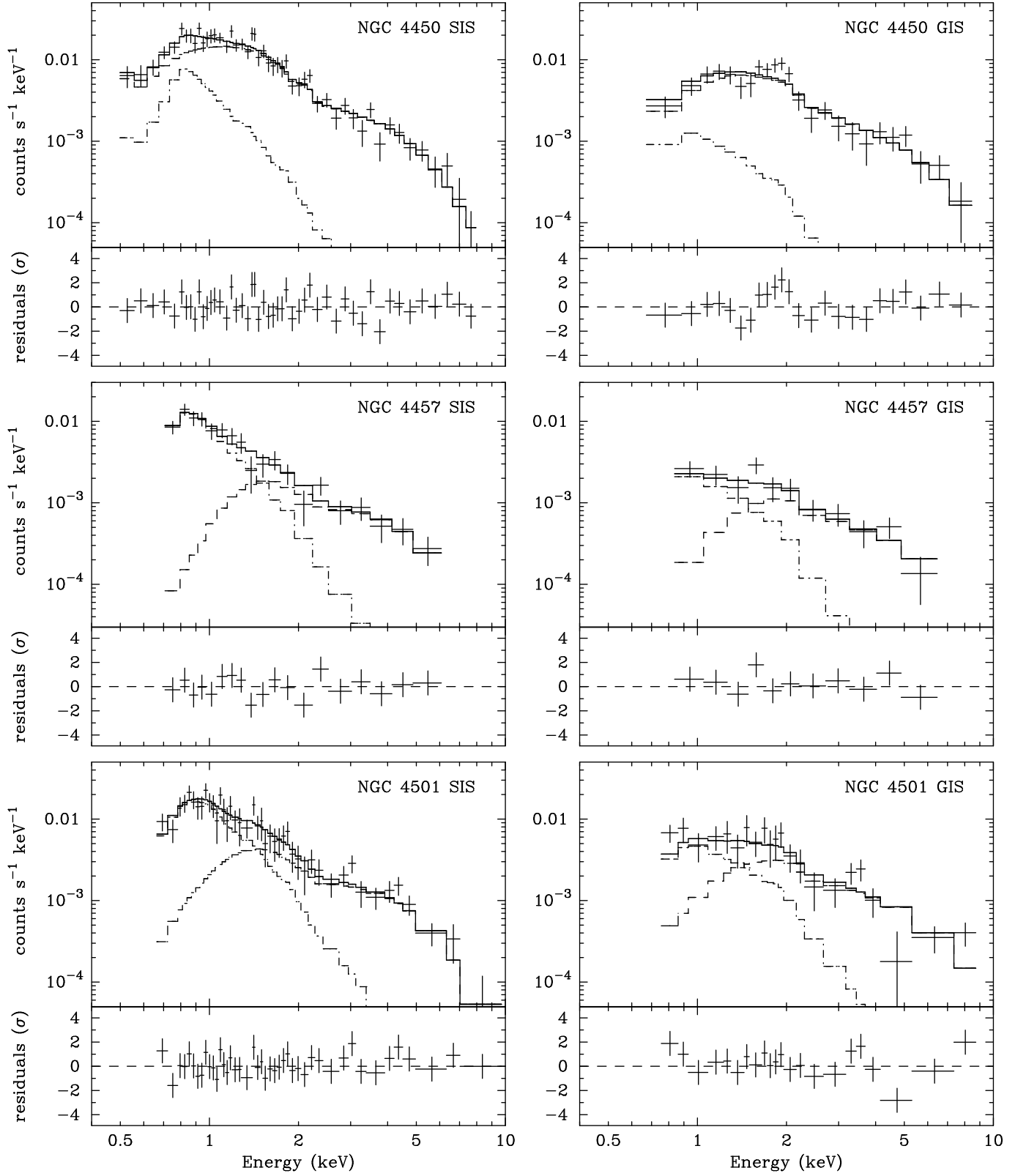


FIG. 1h.— Same as in Figure 1a. (h) NGC 4450 (top), NGC 4457 (middle), NGC 4501 (bottom).

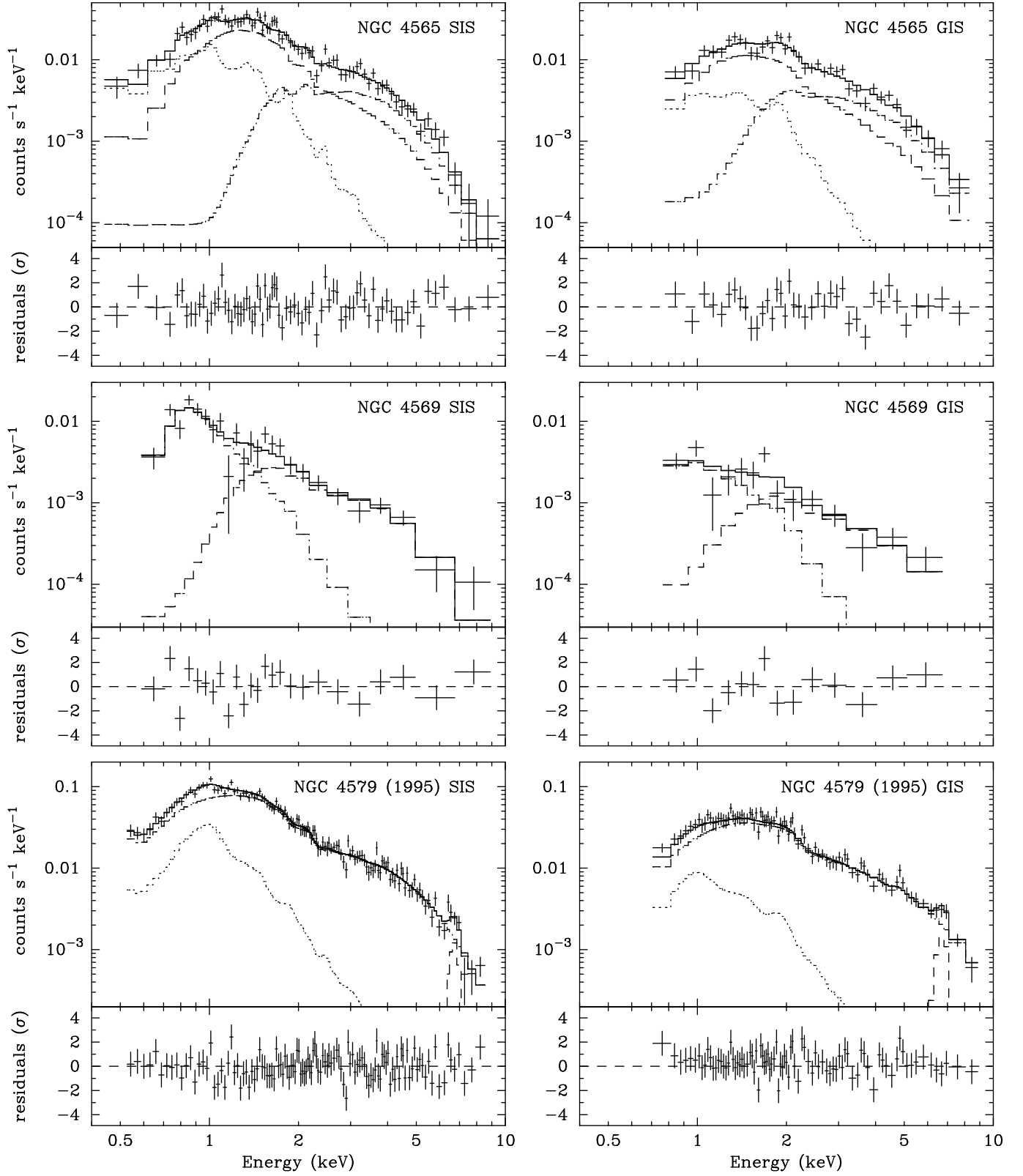


FIG. 1*i*.— Same as in Figure 1*a*. (*i*) NGC 4565 (*top*), NGC 4569 (*middle*), NGC 4579 (1995) (*bottom*).

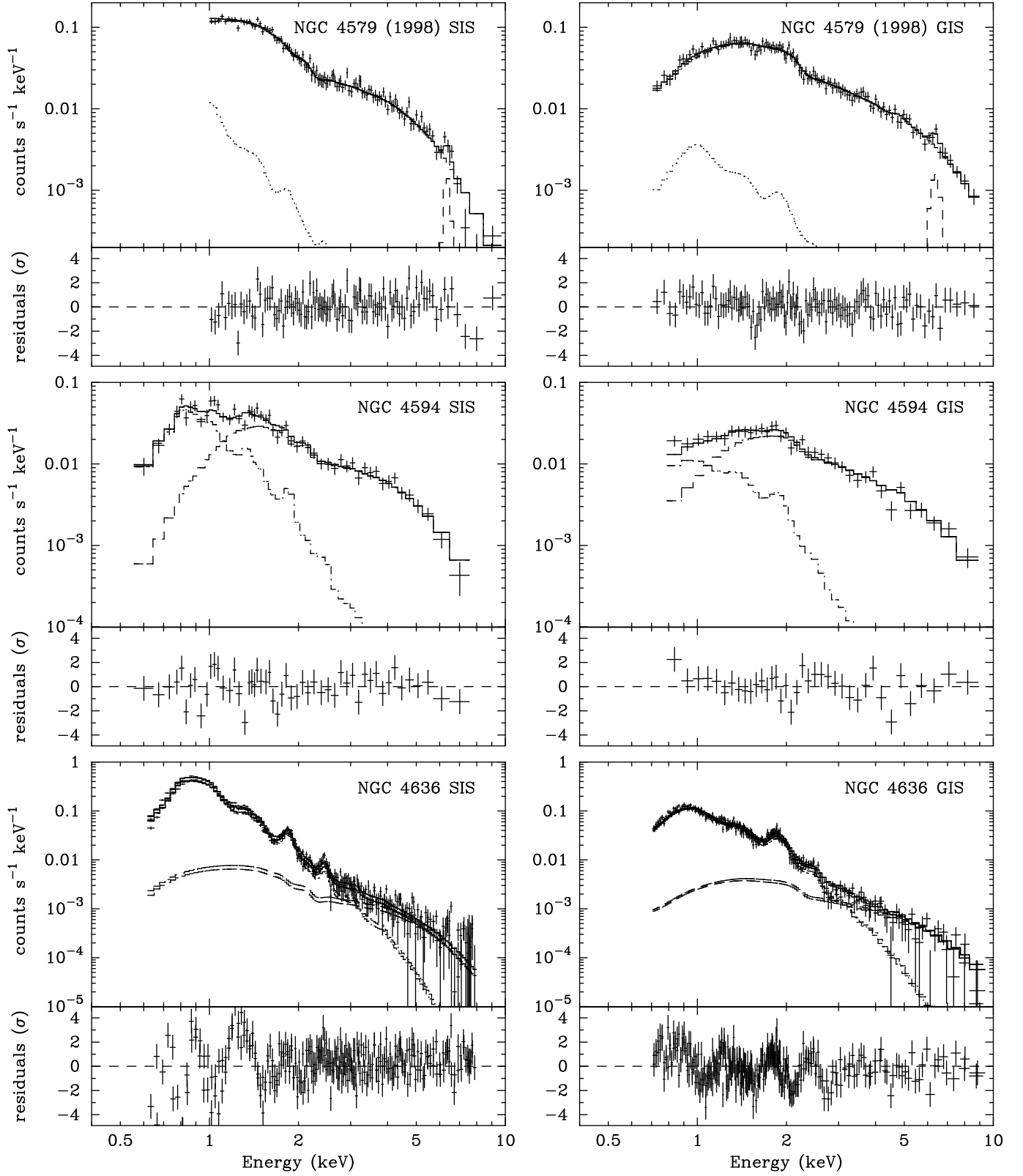


FIG. 1j.— Same as in Figure 1a. (j) NGC 4579 (1998) (top), NGC 4594 (middle), NGC 4636 (bottom).

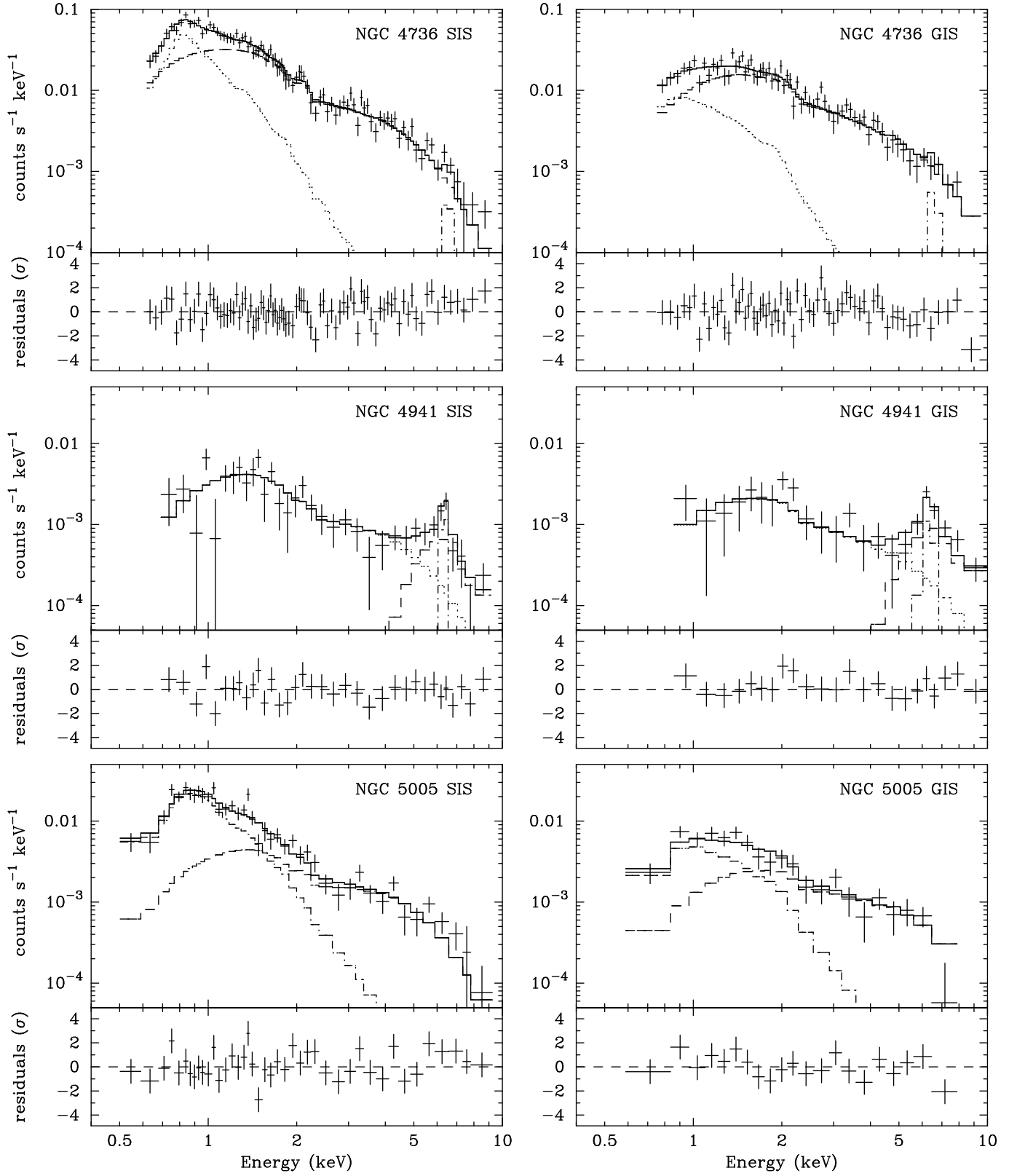


FIG. 1k.— Same as in Figure 1a. (k) NGC 4736 (top), NGC 4941 (middle), NGC 5005 (bottom).

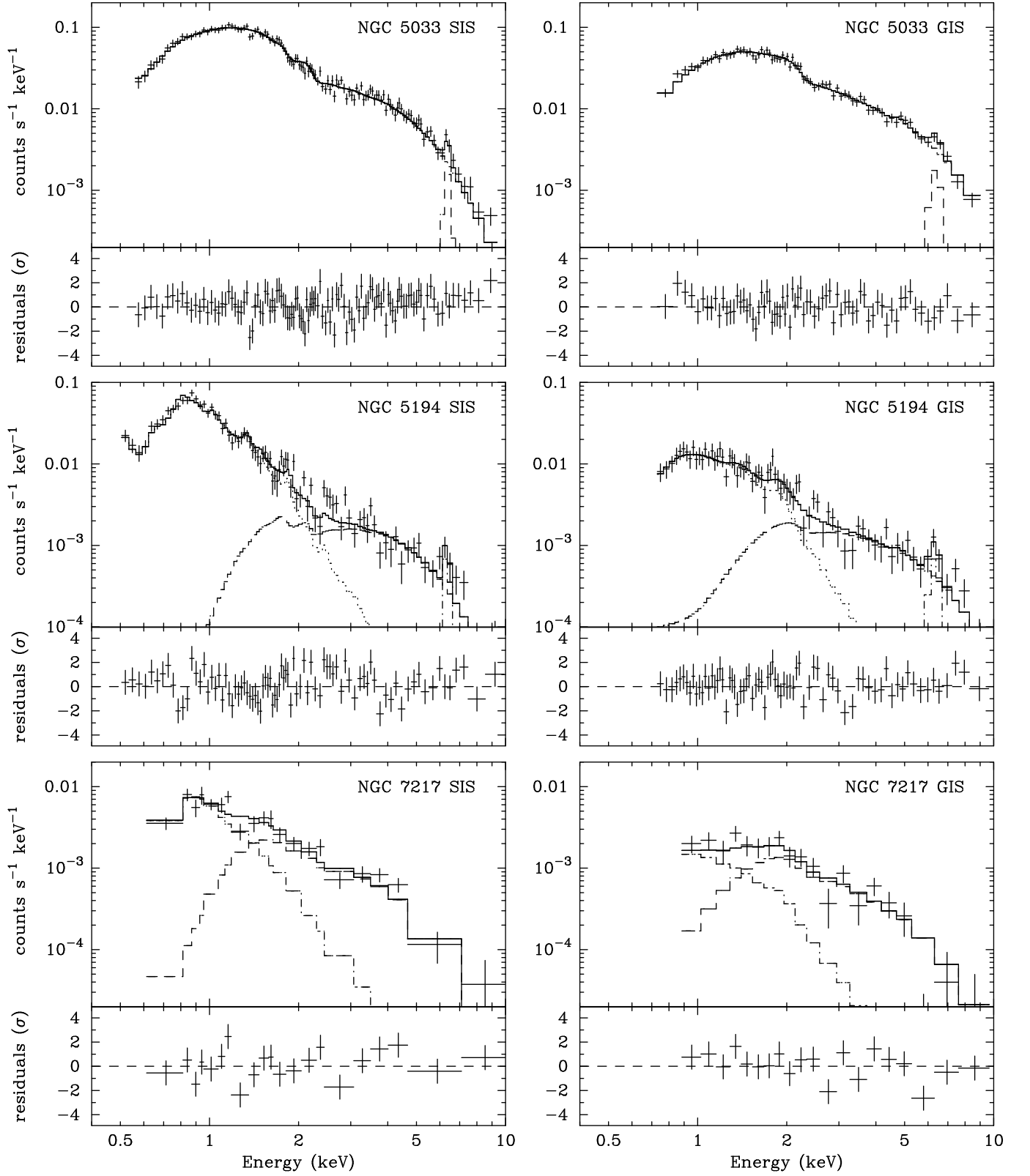


FIG. 11.— Same as in Figure 1a. (*l*) NGC 5033 (*top*), NGC 5194 (*middle*), NGC 7217 (*bottom*).

4.4. Fe K Lines

Tables 9 and 10 summarize the parameters of the Fe K emission line. Adding a Gaussian component to the best-fit continuum model improved the χ^2 values ($\Delta\chi^2 > 3$) for the 16 objects shown in Table 9. The additional parameters in the fit are the center energy, line width, and line intensity. In cases where the photon statistics are limited, we assumed the line to be narrow. For NGC 2639, the line center energy was fixed at 6.4 keV in the source rest frame. Table 10 gives upper limits for the rest of the objects in which the Fe K emission line is not clearly seen.

5. SUMMARY OF THE SPECTRAL RESULTS

We summarize the best-fit models and parameters for all the spectral classes. Tables 11 and 12 present results for the soft and hard components, respectively. These tables show that the spectra of most of the objects analyzed here are well represented by the canonical model and that a small fraction of LINER 1s, Seyfert 1s and Seyfert 2s do not require the soft RS component. Thus, this canonical spectrum appears to be widely applicable to LINERs and LL Seyferts.

Figure 2 shows histograms of the spectral parameters (photon index, absorption column, and temperature for the RS component) for each spectral class. Since the errors of the spectral parameters for many objects are large, we present *weighted* histograms, where the same area of a rectangle is assigned to each data set and the width of the rectangle is the error range in the spectral fits. In generating the histograms of photon indices and absorption column densities, we excluded objects with very low signal-to-noise ratios or cases where the photon index was not well constrained (NGC 404, 1386, 4192, and 7743). The histogram of the temperature of the RS component is created using objects which clearly show the presence of the soft thermal component. The objects for which the temperature was not well constrained were excluded.

The distribution of photon indices for the four spectral classes are similar to each other, although LINER 2s and Seyfert 2s have somewhat broader distribution than LINER 1s and Seyfert 1s. This difference is possibly due to the larger errors in the type 2 objects.

The distributions of the absorption column densities appear different from each other. Very large column densities — in excess of 10^{23} cm^{-2} — are observed in several Seyfert 2s, one LINER 1 (NGC 1052), and one Seyfert 1 (NGC 4258, 1993 observation). No LINER 2s in the present sample are obscured by $N_H > 10^{23} \text{ cm}^{-2}$. We note that in objects with very high columns ($N_H > 10^{24} \text{ cm}^{-2}$), only scattered emission would be seen, and the *apparent* (observed) column densities would be much lower than the true column densities. Such is the situation in NGC 1365 and NGC 5194.

The temperature of the RS component is confined to the range 0.5–0.8 keV. This distribution is similar to that presented by Ptak et al. (1999) for a smaller, more heterogeneous sample of LINERs, Seyferts, and starburst galaxies.

Apart from the absorption column densities, which exhibit greater diversity, the spectral parameters of the LINERs and Seyferts in our sample are rather homogeneous. The canonical model we have adopted, however, can also be applied to starburst galaxies and normal galaxies (e.g., Ptak et al. 1999). The apparent similarity of the spectra, therefore, does not in itself imply that the different classes of objects share the same X-ray production mechanism, nor does it necessarily mean that they are physically related. Recall that, with very few exceptions,

the hard component of the spectral fit could just as well be represented by a power law or a thermal bremsstrahlung model. Therefore, we need to analyze carefully all the available information — morphology, variability, and multiwavelength information — before we can draw firm conclusions regarding the nature of these sources. This is the subject of Paper II.

6. FLUXES AND LUMINOSITIES

The total X-ray fluxes and luminosities, and the respective quantities for the the hard and soft components separately, are listed in Tables 13 and 14. The best-fit model was assumed to calculate them. As for the hard component, we assumed a power law rather than a thermal bremsstrahlung model for all the cases, since the power-law model gave better or similar results compared to a thermal bremsstrahlung model. The total (soft plus hard components) fluxes and luminosities in the 0.5–2 keV and 2–10 keV bands are shown in columns (2) and (3). The observed and absorption-corrected fluxes and luminosities for the power-law component are given in columns (4) and (5) for the 2–10 keV band, and in columns (6) and (7) for the 0.5–4 keV band. Since the estimated fluxes and luminosities of the soft component depend on the assumed abundance, we show two cases (abundance = 0.1 solar and 0.5 solar) if the abundance was assumed in the fits. The fluxes and luminosities of the hard component depend only weakly on the assumed abundance of the soft component.

7. VARIABILITY

X-ray variability is one of the most important characteristics of AGNs. We searched for X-ray variability by inspecting light curves constructed by binning the data to a bin size of 5760 s, one orbital period of ASCA. When observations were performed more than twice, we searched for long-term variability between multiple observations, usually separated by intervals of a week to a few years. We also compared the ASCA luminosities obtained in this paper with published results from observations by other missions. An X-ray variability study of the brighter objects in our sample, concentrating on timescales within a day, has been presented by Ptak et al. (1998) and Awaki et al. (2001).

7.1. Short-term Variability

X-ray variability within each ASCA observation, which has a typical duration of one day, has been detected in NGC 3031 (Ishisaki et al. 1996; Iyomoto & Makishima 2001) and NGC 5033 (Terashima, Kunieda, & Misaki 1999). Other objects showed no significant variability in a single-day observation. A typical upper limit on the root-mean-square amplitude is $\sim 10\%$ for relatively bright objects ($\sim 0.1 \text{ counts s}^{-1} \text{ detector}^{-1}$) and $\sim 50\%$ for faint objects ($\sim 0.03 \text{ counts s}^{-1} \text{ detector}^{-1}$ or less). Short-term variability (less than one day) has been reported in a few objects from *BeppoSAX* observations (NGC 1365, Risaliti, Maiolino, & Bassani 2000; NGC 3031, Pellegrini et al. 2000a; NGC 4258, Fiore et al. 2001).

7.2. Long-term Variability

We searched for long-term variability by comparing X-ray fluxes in multiple ASCA observations. Eleven objects (NGC 404, 1365, 3031, 4111, 4192, 4258, 4438, 4569, 4579, 4639, and 4941) were observed with ASCA more than twice. NGC 3031 (see Ishisaki et al. 1996; Iyomoto & Makishima 2001),

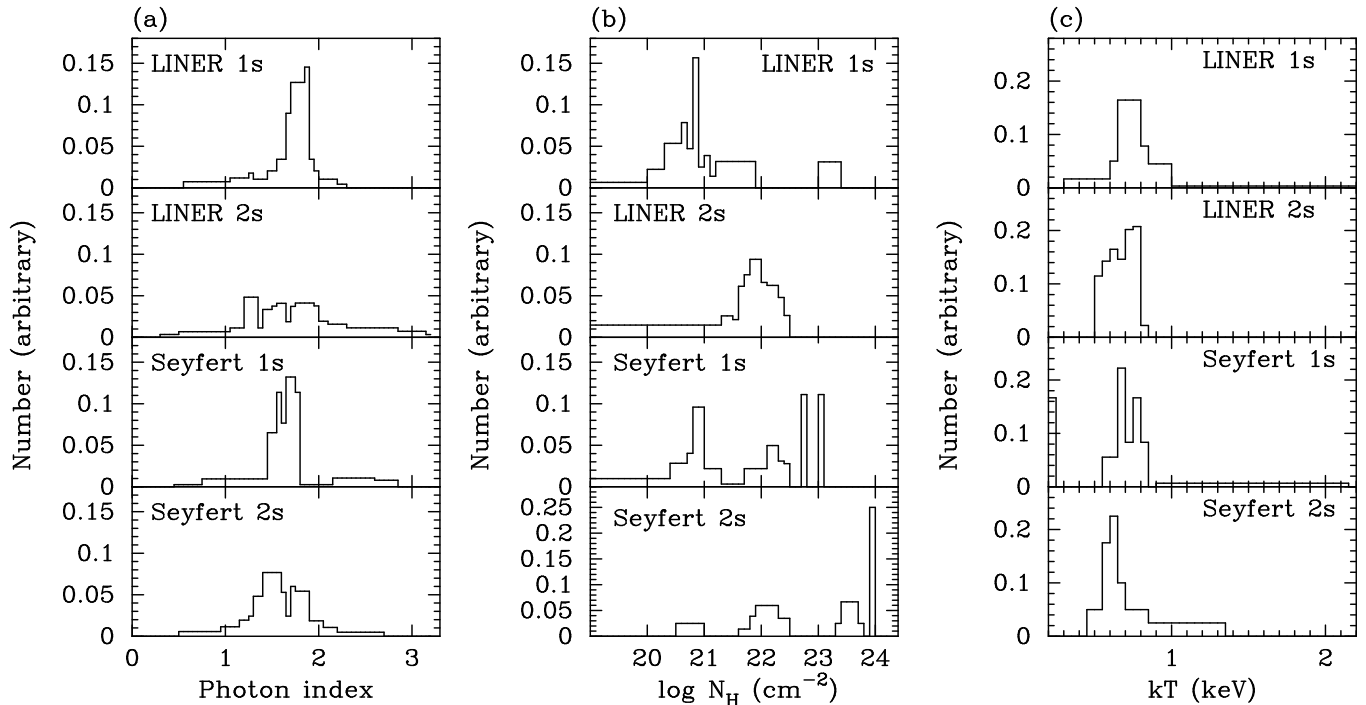


FIG. 2.— Weighted histograms of the best-fit parameters for the whole sample. (a) Photon index. (b) Absorption column density. (c) Temperature of RS plasma.

NGC 4258 (Reynolds, Nowak, & Maloney 2000), and NGC 4579 (Terashima et al. 2000c) show significant variability on timescales of a week to three years. No significant variability was seen in other objects. See Table 2 for count rates in individual observations.

We compared the fluxes obtained here with *ASCA* and those measured with other satellites. Although there are flux measurements in the soft-energy band, it is difficult to compare them with the fluxes in the harder band because of the presence of thermal emission in the soft X-ray band and because of possible calibration uncertainties. Therefore, we used the energy band of 2–10 keV for the comparison. To minimize contamination from extranuclear sources, we used mainly data from imaging detectors, the exceptions being NGC 3998, 5033, and 5194. The 2–10 keV fluxes of NGC 3998 and NGC 5194 were obtained with *Ginga*. NGC 5033 was observed with *EXOSAT*. NGC 1052, 1365, 1386, 2273, 3079, 3998, 4258, 4565, 4941, 5005, and 5194 were observed with *BeppoSAX*. Table 15 provides a summary of these fluxes.

Seven out of these 12 galaxies (NGC 1365, 3031, 3998, 4258, 4941, 5005, 5194) clearly show long-term variability on a timescale of a month to several years. The variability in other objects is not clear, given the uncertainties in calibration and spectral modeling.

8. IMAGE ANALYSIS

Next, we examine whether the X-ray images are consistent with the point-spread function (PSF) of *ASCA*. Only SIS images were used since the combination of SIS and the X-ray telescope (XRT; Serlemitsos et al. 1995) has better spatial resolution than GIS+XRT. In order to compare the observed SIS images with the PSF, we constructed radial profiles of the surface brightness when there is no nearby bright source. Then we fitted the radial profile with a model PSF plus a constant background us-

ing a χ^2 -minimization technique. The free parameters in this fit are the normalization of the PSF and the background level. We also tried to apply a model two-dimensional Gaussian convolved with the PSF plus a constant background to constrain the source extent (technique described in Ptak 1998). The free parameters in this fit are the normalization of the Gaussian, the width of the Gaussian (σ), and the background level. Examples of fits can be found in Ptak (1998) and Terashima et al. (2000b).

In some cases there is a nearby source of nonnegligible brightness compared to the main target. We constructed a one-dimensional projection along the two sources. The one-dimensional profile of the surface brightness was fitted with a model consisting of two PSFs plus a constant background. The peak positions for the two sources were fixed, and the free parameters are the two normalizations of the PSF and the background level. If the main target was clearly extended, we utilize instead a two-dimensional Gaussian convolved with the PSF. The resulting two-dimensional model is then projected into one dimension using the same procedure as applied to the actual data. Figure 3 gives examples of the fits to the one-dimensional projections for NGC 2273 and NGC 4438 in the two energy bands 0.5–2 keV and 2–10 keV. The source 2' south of NGC 2273 (left peak in Fig. 3a and 3b) coincides with the radio source 064542.0+605210 within positional accuracy, but the source near NGC 4438 located at (12^h27^m57.4^s, 13°2'18'') (J2000) (left peak in Fig. 3c and 3d) has no counterpart in NED. The soft-band image of NGC 4438 is extended compared to the PSF, while the hard-band image is consistent with a point source. NGC 2273 is pointlike in both energy bands. The nucleus of NGC 2273 is brighter in the hard band than the adjacent radio source, whose spectrum can be well fitted by a power law with a photon index of 1.9. This fact indicates that the spectrum of NGC 2273 is very hard and in agreement with the results of

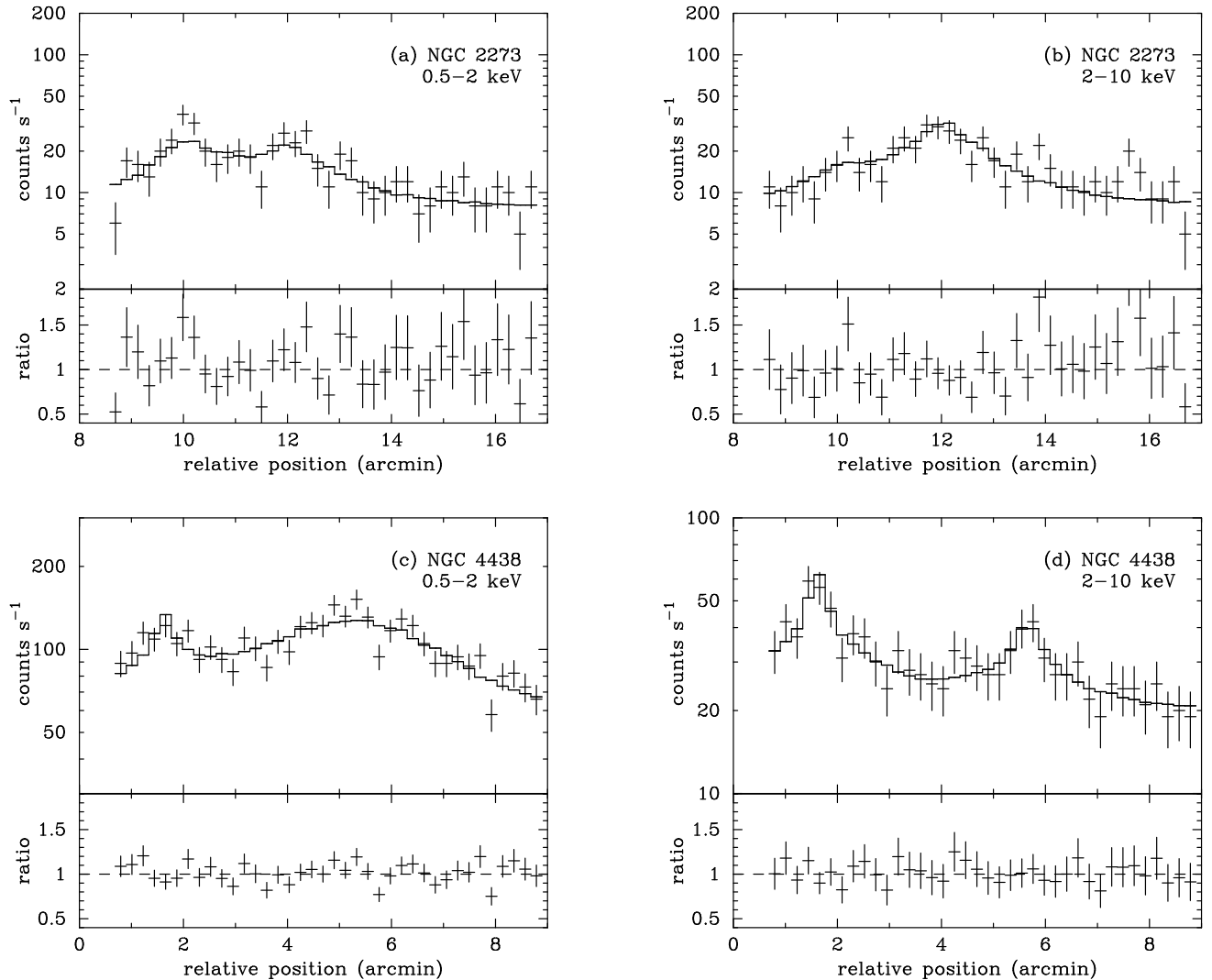


FIG. 3.— Examples of fits to the one-dimensional projection of the surface brightness. The model consists of two PSFs plus a constant background. (a) NGC 2273 in 0.5–2 keV. (b) NGC 2273 in 2–10 keV. (c) NGC 4438 in 0.5–2 keV. (d) NGC 4438 in 2–10 keV.

the spectral fits.

The objects which clearly show extended emission in the hard-energy band are NGC 3607, 4111, 4374, 4569, 4636, 5194, and probably 7217. Some of the objects whose images are consistent with the PSF are faint. We comment on the constraints on the source extent from Gaussian fits in the next section for such objects. Some information from *ROSAT* HRI images and recent *Chandra* observations are given in section 9.

9. NOTES ON INDIVIDUAL OBJECTS

This section presents some notes on individual objects, based mainly on data from the hard X-ray band. The optical spectroscopic classification is given in parentheses after the object name.

NGC 315 (L1.9). — An analysis of the *ASCA* data is presented in Matsumoto et al. (2001). A *ROSAT* HRI image shows a compact core and probably an extended component. The contribution of the point source to the HRI flux depends on

modeling details (Canosa et al. 1999; Worrall & Birkinshaw 2000). Extended emission is seen in the *ROSAT* PSPC image (Worrall & Birkinshaw 2000). The *ASCA* images in the soft and hard bands are consistent with being pointlike.

NGC 404 (L2). — An analysis of the *ASCA* data is presented in Terashima et al. (2000c). No clear X-ray emission was detected in our *ASCA* observations. Komossa et al. (1999) and Roberts & Warwick (2000) reported a *ROSAT* HRI detection with an X-ray luminosity of 5×10^{37} ergs s $^{-1}$ in the 0.1–2.4 keV band. Lira et al. (2000) also reported a similar result. This luminosity is slightly higher than our upper limit which is obtained assuming a power-law spectrum with $\Gamma = 2$. The *ROSAT* detection and luminosity suggest that this source has a softer X-ray spectrum than that we assumed, since *ROSAT* is more sensitive in the softer energy band than *ASCA*. Alternatively the source could have faded since the *ROSAT* observation. No spectral information was obtained from the *ROSAT* observation.

We analyzed a recent 24 ks *Chandra* observation and found

a compact nucleus with a very soft spectrum which is well represented by a thermal plasma model with $kT \approx 0.8$ keV. A hint of a hard component is also seen. If the hard component is modeled by a power law with a photon index of 2.0, the observed flux in the 2–10 keV band becomes $\sim 3 \times 10^{-14}$ ergs $\text{s}^{-1} \text{cm}^{-2}$, which corresponds to a luminosity of 2×10^{37} ergs s^{-1} .

NGC 1052 (L1.9). — *ASCA* results are presented in Guainazzi & Antonelli (1999) and Weaver et al. (1999). Detection of hard X-rays up to ~ 200 keV with *BeppoSAX* is reported in Guainazzi et al. (2000).

A heavily absorbed continuum, which indicates the presence of an obscured AGN, is clearly seen in the *ASCA* spectrum. Systematic undulations in the residuals were seen in the fits using a partially covered power-law model or a RS plus absorbed power-law model. The best-fit model we obtained is a RS plus partially absorbed power-law model. The resulting photon index of $1.67^{+0.57}_{-0.40}$ is similar to those found in luminous AGNs and in other objects presented in this paper. Since the photon index depends on the assumed spectral model (see Tables in this paper and Weaver et al. 1999), the very flat spectral slope obtained by Guainazzi & Antonelli (1999) and Guainazzi et al. (2000) ($\Gamma \approx 1.4$) should be taken with caution. The thermal plasma component in the best-fit model plausibly can be attributed to a hot gaseous halo associated with the elliptical host of NGC 1052.

NGC 1097 (L2/S1.5). — An analysis of the *ASCA* data is presented in Iyomoto et al. (1996). The *ROSAT* HRI image shows a distinct nucleus and weak extended emission due to a circumnuclear star-forming ring (Pérez-Olea & Colina 1996). A recent *Chandra* observation shows that the hard X-ray emission is dominated by the nucleus (Y. Terashima, & A. S. Wilson 2001, private communication).

NGC 1365 (S1.8). — The results of the *ASCA* observations, performed in 1994 August and 1995 January, are presented in Iyomoto et al. (1997). A serendipitous source is detected at $1'5$ SW of the nucleus in the second observation, but the separation is too close to allow the two sources to be separated with GIS, which has a broader PSF than SIS.

Iyomoto et al. (1997) generated five spectra: (1) SIS spectrum of the nucleus in 1994, (2) SIS spectrum of the nucleus in 1995, (3) SIS spectrum of the serendipitous source in 1995, (4) GIS spectrum of the nucleus in 1994, and (5) GIS spectrum of the nucleus plus the serendipitous source in 1995, fitted simultaneously. The spectral models they used were: (a) a sum of a power law, Gaussian, and RS plasma for (1), (2), and (4) (nuclear component), (b) a power law for (3) (serendipitous source), and (c) a sum of the nuclear component and the serendipitous source model for (5). The spectral parameters for SIS and GIS were assumed to be same. No spectral variability was assumed between the 1994 and 1995 observations.

We applied a similar technique to fit both the nucleus and the serendipitous source. We fitted the three spectra (SIS spectrum of the nucleus [(1)+(2)], SIS spectrum of the serendipitous source (3), and GIS spectrum of the nucleus plus the serendipitous source [(4)+(5)]) simultaneously. The radii used to extract the spectra are the same as those in Iyomoto et al. (1997). In the present analysis, the background spectra were extracted from a source-free region in the same field of view. Various models were examined for the AGN component, as in the other galax-

ies. The best-fit model consists of a power law, a Gaussian, and a RS component. We confirmed the presence of a strong Fe line ($\text{EW} = 1.9^{+1.0}_{-0.8}$ keV) at a center energy higher than 6.4 keV ($6.59^{+0.04}_{-0.05}$ keV).

The X-ray flux obtained in a later *BeppoSAX* observation (Risaliti et al. 2000) is higher by a factor of 6 compared to *ASCA*, and an absorbed ($N_{\text{H}} = 4 \times 10^{23} \text{ cm}^{-2}$) direct continuum from the nucleus appeared. The Fe line center energy in the *BeppoSAX* observation is slightly lower than 6.4 keV.

A soft-band image obtained with the *ROSAT* HRI may be extended compared to the PSF (Stevens, Forbes, & Norris 1999; but see also Komossa, & Schultz 1998). Plausible origins of the soft component are soft thermal gas due to starburst activity or scattered emission from the AGN.

NGC 1386 (S2). — Detailed results are discussed in Iyomoto et al. (1997). In the NGC 1386 field, non-uniform diffuse emission due to the Fornax cluster is seen. In the present paper, we measured the temperature and brightness of the cluster component using a region which is located the same distance from the cluster center as is NGC 1386, and then added it to the spectral model instead of subtracting it from the data in order to improve the photon statistics.

A power law absorbed with $N_{\text{H}} = 4.5 \times 10^{23} \text{ cm}^{-2}$ is seen in our *ASCA* spectrum. Maiolino et al. (1998), on the other hand, modeled the *BeppoSAX* spectrum of this source using a cold reflection model. The difference in spectral models, however, does not necessarily imply true spectral variability, because the photon statistics of the *BeppoSAX* spectrum are very limited.

NGC 2273 (S2). — There is a serendipitous source $2'$ south of NGC 2273 in both the SIS and GIS images. The position of this source coincides with the radio source 064542.0+605210. We extracted SIS spectra of NGC 2273 and this radio source using circular regions with a radius of $1'5$ and $1'0$, respectively. We made one GIS spectrum using an extraction radius of $4'$ which contains both sources since the separation is too small to be resolved with the GIS. These three spectra were fitted simultaneously. The models applied are (a) a partially covered power-law model with two Gaussians (Fe $K\alpha$ and Fe $K\beta$) modified by absorption along the line of sight for the SIS spectrum of NGC 2273, (b) an absorbed power-law for the SIS spectrum of the radio source, and (c) a combination of (a) and (b) for the GIS spectrum. The normalizations for the SIS model and GIS model were fitted separately, while the other spectral parameters were tied. The ratio of the normalizations of the two sources for GIS was assumed to be same as those of SIS. The results of the fits are shown in Table 4. The best-fit spectral parameters for the radio source are $\Gamma = 1.85^{+0.30}_{-0.24}$, $N_{\text{H}} = 0$ ($< 7.0 \times 10^{20} \text{ cm}^{-2}$), and $f(2-10 \text{ keV}) = 1.2 \times 10^{-13} \text{ ergs s}^{-1} \text{cm}^{-2}$. In Figure 1b, the steeper power law corresponds to the spectrum of the radio source.

The spectrum of NGC 2273 shows a heavily absorbed continuum ($N_{\text{H}} = 1.1 \times 10^{24} \text{ cm}^{-2}$) and a strong fluorescent Fe K line with $\text{EW} = 1.0$ keV. The large EW of the Fe line indicates that the hard X-ray emission is dominated by reflection from cold material. Our modeling of the continuum shows that transmitted emission through a column density of 10^{24} cm^{-2} is also present. We tried a pure reflection component instead of a heavily absorbed power law, but this gave a worse fit ($\Delta\chi^2 = +16$). Maiolino et al. (1998) detected a strong ($\text{EW} = 3.8 \pm 1.1$ keV) fluorescent Fe K line using *BeppoSAX*, and they

suggested that the source contains a significant cold reflection component. Pappa et al. (2001) recently analyzed the same ASCA data set. Their preferred model is consistent with ours, although our spectrum has better signal-to-noise ratio because we used a larger extraction radius for the GIS data.

NGC 2639 (S1.9). — ASCA observations of this Seyfert 1.9 galaxy were published by Wilson et al. (1998). We used SIS0+SIS1 and GIS2+GIS3 spectra, while Wilson et al. fitted only GIS3 and SIS1 because of a large offset angle from the optical axis for GIS2 and SIS0 data. Inclusion of data from all the detectors improved the photon statistics, particularly in the low-energy band which strongly affects the power-law slope. The best fit was achieved with a partially covered power-law model. The derived photon index is somewhat steeper than normal for Seyferts, perhaps an indication of the presence of an additional soft component. Therefore, we tried a model consisting of a power law plus a RS thermal plasma. The abundance of the RS component was assumed to be 0.1 or 0.5 solar, and a Gaussian line was added. This model also successfully reproduced the observed spectrum. In this case, however, a heavily absorbed component is not necessary. On the other hand, the large EW (> 1.1 keV) of the Fe emission line suggests that the nucleus is highly obscured. The observed hard emission thus can be interpreted as scattered emission. If this is the case, the intrinsic luminosity should be one or two orders of magnitude higher than the observed luminosity.

NGC 2655 (S2). — The ASCA spectrum of this Seyfert 2 galaxy clearly shows the presence of a heavily absorbed component and an additional soft component. A RS + power-law model fit gave a negative photon index. Although such a very flat spectral slope is expected from “cold” reflection, the lack of a strong Fe K fluorescent line rules out this possibility. Therefore, we tried three alternative models: a partially covered power-law model, a double power-law model, and a RS + partially covered power-law model. The best-fit photon index in the partially covering model ($\Gamma = 2.6$) is steeper than the canonical slope of Seyfert galaxies. This slope is primarily determined by the soft-energy band, which has better photon statistics, and suggests that there exists a softer component in addition to a hard power law from the AGN. If we adopt a double power-law model, the photon index of the soft component becomes $\Gamma = 2.4$, where we fixed the photon index of the hard component at $\Gamma = 2.0$. In this model, the absorption column density for the hard component is $N_H = 4.0 \times 10^{23} \text{ cm}^{-2}$. Finally, we tried to add a RS component to a partial covering model. We assumed a temperature of $kT = 0.65$ keV and an abundance of 0.1 solar since these parameters were not well constrained. The absorption column densities for the RS component and the less absorbed power law were assumed to be equal to the Galactic value. The model improved by $\Delta\chi^2 = -16.3$ for one additional parameter (normalization of the RS component) compared to a partial covering model. The best-fit photon index and absorption column are $\Gamma = 1.26^{+0.57}_{-0.69}$ and $N_H = 4.5^{+2.0}_{-1.4} \times 10^{23} \text{ cm}^{-2}$.

NGC 3031 (S1.5). — ASCA observed this galaxy many times; see Iyomoto and Makishima (2001), who analyzed 16 data sets, for the observation log and a timing analysis. Ishisaki et al. (1996) presented detailed results of the observations between 1993 May 1 to 1995 April 1, while Serlemitsos et al. (1996) describe three observations done on 1993 April 16, April 25,

and May 1.

We present a combined spectrum of the three observations performed on 1994 October 21, 1995 April 1, and 1995 October 24 (observations #9, 10, and 11 in Iyomoto & Makishima 2001). More recent observations were made using unusual observation modes (lower spectral and spatial resolution but higher timing resolution for GIS). In the earlier observations, the nearby source SN 1993J was bright, and we therefore omitted these in the present analysis.

In our spectral fits, we discarded the energy range below 1 keV for the SIS data since the spectra of the SIS and GIS deviate in this energy range, most likely because of a calibration problem of the SIS in the soft-energy band. This problem is visible only in bright objects such as NGC 3031, and possibly NGC 4579 and NGC 5033.

A soft thermal component is not clearly seen in our spectra presumably due to the brighter hard component in our spectrum, and we assumed the temperature obtained by Ishisaki et al. (1996). The width of the Gaussian component for the Fe line was assumed to be narrow since the line width was not well constrained. The broad ($\sigma \approx 0.2$ keV) or possibly multiple-component Fe line previously reported by Ishisaki et al. (1996) and Serlemitsos et al. (1996) is not clearly seen in our spectra, presumably due to the limited photon statistics. The *BeppoSAX* observation of Pellegrini et al. (2000b) gave upper limits of 0.3 keV for the width of an Fe line. The line centroid energy and EW we obtained are consistent with the ASCA results by Ishisaki et al. (1996) and Serlemitsos et al. (1996) and the *BeppoSAX* results of Pellegrini et al. (2000b). Pellegrini et al. (2000b) obtained an upper limit of 42 eV for the EW of an Fe line at 6.4 keV.

NGC 3079 (S2). — ASCA results are presented in Ptak et al. (1999) and Dahlem, Weaver, & Heckman (1998). Although hard X-ray emission is detected, we found no clear evidence for the presence of an AGN from the present data. The small $L_X/L_{H\alpha}$ ratio (Terashima et al. 2000a) indicates that the AGN component, if the dominant ionizing source of the optical emission lines, should be heavily obscured in the energy band below 10 keV. The upper limit on the EW of an Fe K emission line is large (~ 2 keV), not inconsistent with a highly obscured nucleus. A recent *BeppoSAX* observation detected a strong Fe K emission line and highly absorbed hard X-ray emission (Iyomoto et al. 2001). Such a spectral shape gives clear evidence for the presence of a heavily obscured AGN.

The low-energy portion of the ASCA spectrum shows strong emission lines arising from α -processed elements, which are most likely associated with hot gas arising from powerful starburst activity. A variable abundance model gives a significantly better fit than the solar case ($\Delta\chi^2 = -16.3$).

The absorption column for the hard component depends on the model adopted for the soft component. Our best-fit value is $N_H = 1.7^{+1.8}_{-1.2} \times 10^{22} \text{ cm}^{-2}$. Dahlem et al. (1998) used a two-temperature MEKAL plasma plus a partially covered power law and obtained $N_H = 6 \times 10^{22} \text{ cm}^{-2}$. Ptak et al. (1999), assuming a RS + power-law model, derived a very small column, with a typical upper limit of $N_H \approx \text{few} \times 10^{22} \text{ cm}^{-2}$. Since the hard component seen by ASCA is probably a combination of scattered emission from the AGN and contributions from the starburst region (X-ray binaries, supernovae, and hot gas), the amount of absorption to be attributed to the AGN is highly ambiguous.

NGC 3147 (S2). — A detailed analysis of the *ASCA* data is given in Ptak et al. (1996). We confirmed their detection of a strong Fe K emission line. Although this object is optically classified as a Seyfert 2 galaxy, no strong absorption is seen in the X-ray spectrum. The relatively strong Fe K emission line ($EW = 490^{+220}_{-230}$ eV) could be an indication that the observed X-rays are scattered emission and that the nucleus is obscured below 10 keV. However, the $L_X/L_{H\alpha}$ ratio (32) falls in the range of unobscured AGNs. The ratio of X-ray to [O III] $\lambda 5007$ luminosity is also typical of those observed in Seyfert 1 nuclei (Bassani et al. 1999). Some LLAGNs with low absorption in our sample also show similarly large EWs for the Fe line (~ 300 eV). For example, the X-rays from NGC 4579 ($EW = 490$ eV) and NGC 5033 ($EW = 306$ eV) must be dominated by direct emission because the sources are variable. This suggests that NGC 3147, too, could be largely unobscured. Future observations to search for variability or emission lines due to a scattering medium are crucial to distinguish between these two competing possibilities.

NGC 3507 (L2). — This object is very faint, and a power-law model describes the spectrum well. By adding a RS component, the fit improved by $\Delta\chi^2 = -3.2$ for one additional parameter (normalization of the RS component); we assumed a temperature of $kT = 0.65$ keV and an abundance of 0.1 solar because the photon statistics are inadequate to constrain these parameters. The image in the 2–10 keV band is consistent with the PSF, although the constraint is not tight. A Gaussian fit to the observed image yielded $\sigma = 0.5^{+0.8}_{-0.5}$ arcmin.

NGC 3607 (L2). — The soft and hard band images (0.5–2 keV, 2–7 keV, 4–10 keV) are clearly extended compared to the PSF. We found no clear evidence for the presence of an AGN in this LINER 2. The probable origin of the extended hard X-ray emission is discrete sources in the host galaxy. The hot gas in this elliptical galaxy has been analyzed by Matsushita et al. (2000).

NGC 3998 (L1.9). — *ASCA* results are presented in Ptak et al. (1999). An Fe K line is marginally detected at 6.4 keV. A recent *BeppoSAX* observation (Pellegrini et al. 2000a) has shown that the spectrum from 0.1 to 100 keV is well represented by a power law. The Fe K line was not detected in the *BeppoSAX* spectrum to an EW upper limit of 40 eV.

NGC 4192 (T2). — An analysis of the *ASCA* data is presented in Terashima et al. (2000c). Since the object is very faint, we estimated its spectral shape using the hardness ratio (2–7 keV)/(0.5–2 keV). Assuming the Galactic absorption and a power-law spectrum, we obtain a photon index of ~ 1.7 .

NGC 4203 (L1.9). — An analysis of the *ASCA* data is presented in Iyomoto et al. (1998). There exists a serendipitous source located $2'$ SE of the nucleus of NGC 4203. In the present analysis, we extracted the SIS and GIS spectra using a circular aperture with a radius of $1/2$ and $1/5$, respectively. *ROSAT* PSPC and HRI images show a nucleus as well as some extended emission (Halderson et al. 2001). The *Chandra* image published by Ho et al. (2001) is dominated by the nucleus.

NGC 4258 (S1.9). — We analyzed four *ASCA* observations ob-

tained in 1993 and 1996. Makishima et al. (1994) reported the discovery of an obscured X-ray nucleus using the 1993 observation; Ptak et al. (1999) also discussed the same data set. We reanalyzed this data set in greater detail, as well as three others taken in 1996. Reynolds, Nowak, & Maloney (2000) performed a deep (~ 200 ks) observation in 1999.

The *ASCA* spectrum from 1993 is very complex. In the following fits, we assume the Galactic absorption column density for the soft thermal components. We examined the canonical model which consists of a soft thermal plasma and a hard component. This simple model failed to explain many of the emission lines seen in the region 0.5–3 keV as well as the broad-band continuum shape. A single-temperature fit to the soft X-ray spectrum resulted in $kT \approx 0.65$ keV, but residuals remained near the locations of the H-like O K, He-like and H-like Mg K, and Fe L emission lines in region 0.7–1.4 keV. This suggests that the plasma has multiple components, with temperatures cooler and hotter than 0.65 keV, or that a temperature gradient is present. Therefore, we tried a model composed of a two-temperature RS plasma plus a hard component. This model gave a better fit to the soft thermal emission. However, systematic convex-shaped residuals remained in the 3–10 keV region, which can be attributed to a deficit in the model around 2–3 keV and to an N_H value too small and a photon index (for the hard component) too steep at the χ^2 minimum. A satisfactory fit can be achieved with a model consisting of a two-temperature RS plasma, a thermal bremsstrahlung component, and an absorbed power law. The abundances of the two RS components were assumed to be identical. The temperature of the thermal bremsstrahlung component was fixed at 4 keV. An Fe line is seen at $6.66^{+0.20}_{-0.07}$ keV (source rest frame) with $EW = 108^{+73}_{-64}$ eV. The spectral parameters for the AGN continuum are consistent with those derived by Makishima et al. (1994) based on the GIS data only. Note that Ptak et al. (1999) used the canonical model and obtained a photon index of ~ 1.2 and $N_H \approx 7 \times 10^{22}$ cm $^{-2}$. This model resulted in significant systematic residuals (see Figs. 2*q* and 2*r* in Ptak et al. 1999), suggesting that the true photon index should be steeper and N_H larger.

The complicated soft thermal emission in NGC 4258 is probably due to the superposition of its extended galactic halo and interstellar medium, which is shock heated by the complex system of jets emanating from the nucleus (Pietsch et al. 1994; Cecil, Wilson, & De Pree 1995). A possible origin for the medium-hard emission we modeled with a $kT = 4$ keV thermal bremsstrahlung component might be the integrated emission from low-mass X-ray binaries. Future X-ray spectroscopy with better spatial resolution will be able to resolve these multiple X-ray emission components (see, e.g., Wilson, Yang, & Cecil 2001 for a *Chandra* image).

NGC 4258 was observed three times in 1996 (see Table 2). We fitted the combined spectrum of these three data sets, after discarding the low-energy (< 0.7 keV) portion of the SIS data to minimize calibration uncertainties. The *ASCA* spectrum is well fitted with the canonical model. The flux of the hard component is about twice that observed in 1993, and the energy band above 2 keV is now dominated by the AGN emission. This variability provides additional evidence for the presence of an LLAGN. The medium-hard component introduced to fit the 1993 spectrum was not required for the 1996 data. The soft component can be represented by a single-temperature RS model, in contrast to the 1993 result. This is probably attributable to (1) the degraded energy resolution of the SIS, (2)

the limited energy band used in the spectral fits, and (3) the brighter hard component in 1996. The absorption column for the AGN component decreased from $N_{\text{H}} = 1.3 \times 10^{23} \text{ cm}^{-2}$ in 1993 to $7 \times 10^{22} \text{ cm}^{-2}$ in 1996. An Fe emission line is detected at $6.31^{+0.09}_{-0.10} \text{ keV}$ (source rest frame) with $\text{EW} = 54^{+25}_{-27} \text{ eV}$. The line centroid energy decreased from 6.66 keV to 6.31 keV in the interval of three years, while the continuum luminosity increased during the same period. A similar behavior of Fe line variability has been reported for NGC 4579 (Terashima et al. 2000c). The Fe line energy and EW measured by *BeppoSAX* are $6.57 \pm 0.20 \text{ keV}$ and $85 \pm 65 \text{ eV}$, respectively, but it is unclear whether these values are different compared to those measured with *ASCA*.

NGC 4261 (L2). — An *ASCA* spectrum is presented in Sambruna, Eracleous, & Mushotzky (1999) and Matsumoto et al. (2001). This FR I radio galaxy has a pointlike hard X-ray source with a relatively high X-ray luminosity. The $L_{\text{X}}/L_{\text{H}\alpha}$ ratio of this type 2 LINER suggests that it is predominantly ionized by an LLAGN (see Paper II). Sambruna et al. (1999) claimed that they marginally detected an Fe K line. They assumed a rest energy of 6.4 keV in their spectral fits. On the other hand, Matsumoto et al. (2001) obtained only an upper limit of $\text{EW} = 400 \text{ eV}$. We fitted the Fe line in our *ASCA* spectrum with a free line centroid energy. The line energy we obtained, $E = 6.85^{+0.08}_{-0.15} \text{ keV}$, is higher than observed in luminous AGNs (typically $E \approx 6.4 \text{ keV}$).

The soft-band image is extended to $r > 20'$ and is most likely sampling emission associated with the elliptical host and the galaxy group of which NGC 4261 is a member. In the spectral fits, we made a background spectrum using an annular region around the nucleus in which diffuse emission is clearly present. The soft X-ray flux presented here, therefore, should be regarded as a lower limit to the true flux from the diffuse component. The radial surface brightness profile of the soft-band image is not well fitted by a model consisting of a Gaussian plus a constant background. This is probably due to the presence of bright soft X-ray emission from the elliptical host galaxy and the surrounding group. The χ^2 value for the fit of the 2–10 keV image is also poor, probably for the same reason. The 4–10 keV image, by contrast, is consistent with the PSF. Inspection of archival *Chandra* data shows that the hard-band image indeed is dominated by the nucleus and that the soft-band image is extended.

NGC 4374 (L2). — The X-ray images in the soft and hard bands are clearly extended. The contribution of the AGN to the hard emission should be small; this is confirmed by the *Chandra* of Ho et al. (2001). The most likely origin of the extended hard emission is X-ray binaries in the host galaxy, as discussed in Matsushita et al. (1994). The hot gas component in this elliptical galaxy has been analyzed by Matsumoto et al. (1997), Buote & Fabian (1998), and Matsushita et al. (2000).

NGC 4438 (L1.9). — The LINER 1.9 nucleus of this galaxy is a very weak X-ray source. The image in the 2–10 keV band is consistent with the PSF, while the 0.5–2 keV image is clearly extended. The *ROSAT* HRI image is also extended (Halderson et al. 2001). The $L_{\text{X}}/L_{\text{H}\alpha}$ ratio (0.8) is too low to account for the optical line emission, unless the nucleus is heavily obscured at energies above 2 keV.

NGC 4450 (L1.9). — The *ROSAT* PSPC image is dominated by a pointlike nucleus (Halderson et al. 2001). The serendipitous source seen in the PSPC image ($\sim 3'$ NE of the nucleus, Komossa et al. 1999) is not clearly present in the *ASCA* data.

NGC 4501 (S2). — The image in the 0.5–2 keV band is extended. A Gaussian fit to the radial profile yielded $\sigma = 1.0 \pm 0.4$ arcmin. In the hard band (2–10 keV and 4–10 keV), the radial profiles are consistent with the PSF ($\sigma = 0.7 \pm 0.4$ and $0.6^{+1.3}_{-0.6}$ arcmin, respectively). The *ROSAT* HRI image is extended (Halderson et al. 2001). The X-ray spectrum shows no indication of significant absorption ($N_{\text{H}} < 2.3 \times 10^{22} \text{ cm}^{-2}$), and there is no strong evidence for Fe K emission (adding a narrow Gaussian at 6.4 keV gives $\Delta\chi^2 = -2.9$), although the EW upper limit is large ($< 2310 \text{ eV}$). The $L_{\text{X}}/L_{\text{H}\alpha}$ ratio (17) lies in the range for unobscured AGNs (Terashima et al. 2000a). These facts suggest that this Seyfert 2 galaxy is not heavily obscured in the X-ray band. Alternatively, it is possible that the hard X-ray emission comes mainly from X-ray binaries, whatever contribution from an obscured AGN being strongly diluted, as in the case of NGC 5194 (Terashima et al. 1998b; Terashima & Wilson 2001; Fukazawa et al. 2001).

NGC 4565 (S1.9). — Mizuno et al. (1999) presented *ASCA* results for NGC 4565. The nucleus and an off-nuclear source 0.8 arcmin away, previously detected with *ROSAT* (PSPC: Vogler, Pietsch, & Kahabka 1996; HRI: Mizuno et al. 1999, Halderson et al. 2001), are seen in the *ASCA* SIS images, but they are not resolved in the GIS images. The source coincident with the nucleus appears pointlike in a *ROSAT* HRI image (Halderson et al. 2001). The off-nuclear source is ~ 2 times brighter than the nucleus. As the spatial resolution of *ASCA* is insufficient to resolve the two sources, we extracted a single spectrum for both sources. Among the models we examined, the most successful fit was obtained with a partially covered power law plus a RS plasma. A partial covering model without the RS component yielded a slightly worse result ($\Delta\chi^2 = +4.6$). A simple power-law model seems inappropriate in view of the systematic, wavy residuals it generated. We also attempted a multicolor-disk blackbody model (Mitsuda et al. 1984), which was examined by Mizuno et al. (1999), and obtained results consistent with theirs. The best-fit parameters for this model are $kT_{\text{in}} = 1.49 \pm 0.08 \text{ keV}$ and $N_{\text{H}} = 1.2^{+2.5}_{-1.2} \times 10^{20} \text{ cm}^{-2}$; $\chi^2 = 151.4$ for 112 dof.

Inspection of the one-dimensional projected profiles in the hard and soft-energy bands shows that the two sources have similar spectral hardness. Thus, the nucleus and the off-nuclear source each contributes about one-third and two-thirds, respectively, to the total luminosity ($1.8 \times 10^{40} \text{ ergs s}^{-1}$). The intrinsic luminosity depends on the assumed model. Tables 13 and 14 show the intrinsic flux and luminosity for the case of a partially covered power law plus RS model.

Mizuno et al. (1999) interpreted that both sources are luminous accreting black hole binaries (see also Makishima et al. 2000). They suggest that the derived absorption column density ($N_{\text{H}} < 2 \times 10^{21} \text{ cm}^{-2}$) is too low for the nucleus of an edge-on galaxy. We argue that an LLAGN is a likely origin for the nuclear source. First, the nucleus shows an optical spectrum classified as a type 1.9 Seyfert (Ho et al. 1997a). The detection of broad $\text{H}\alpha$ emission provides strong support for the presence of an AGN. Second, the $L_{\text{X}}/L_{\text{H}\alpha}$ ratio (20) is in good agreement with those of LLAGNs and luminous AGNs

(Terashima et al. 2000a). Third, the internal reddening determined from the Balmer decrement, $E(B-V)_{\text{int}} = 0.47$ mag (Ho et al. 1997a), corresponds to $N_{\text{H}} = 2.7 \times 10^{21} \text{ cm}^{-2}$ for the conversion $E(B-V) = N_{\text{H}}/(5.8 \times 10^{21} \text{ cm}^{-2}) \text{ mag}$ (Bohlin, Savage, & Drake 1978). This value of N_{H} is consistent with the mild absorption observed in the X-ray spectrum. Finally, the radio properties further support the AGN interpretation: the nucleus contains a compact radio core which has a flat spectrum (Nagar et al. 2000; Falcke et al. 2000) and is variable (Falcke et al. 2001; Ho & Ulvestad 2001). Further X-ray observations with higher spatial resolution would be extremely useful.

NGC 4569 (T2). — Detailed analysis of an *ASCA* observation is presented in Terashima et al. (2000c). The *ASCA* image in the hard band (2–7 keV) is clearly extended compared to the PSF. This implies that the luminosity of the nucleus (before correction for absorption) is much lower than the observed luminosity. The recent *Chandra* observation of Ho et al. (2001) shows that the nucleus is surrounded by other sources of comparable brightness; for a power-law spectrum with $\Gamma = 1.8$ and $N_{\text{H}} = 2 \times 10^{20} \text{ cm}^{-2}$, the X-ray luminosity of the nucleus is $2.6 \times 10^{39} \text{ ergs s}^{-1}$ in the 2–10 keV band. This luminosity is about a factor of 4 smaller than the *ASCA* luminosity in the same energy band.

NGC 4579 (S1.9/L1.9). — Detailed analyses of three *ASCA* observations are presented in Terashima et al. (1998a, 2000c). A *Chandra* image in the hard band is dominated by the nucleus (Ho et al. 2001).

NGC 4594 (L2). — *ASCA* results are briefly discussed in Nicholson et al. (1998). These authors reported that adding an RS component to the power-law model did not affect the fit appreciably. By contrast, we find that adding an RS component significantly improves the fit ($\Delta\chi^2 = -33.8$ for three additional parameters). Our result agrees well with the independent analyses of the same data set by Serlemitsos et al. (1996), Ptak et al. (1999), and Roberts, Schurch, & Warwick (2001). Fabianno & Juda (1997) and Roberts et al. (2001) detected a nuclear point source which dominates the soft X-ray luminosity in the *ROSAT* HRI image. A *Chandra* image in the hard band is dominated also by the nucleus (Ho et al. 2001).

NGC 4636 (L1.9). — NGC 4636 was observed with *ASCA* in 1993 and 1995–1996. We analyzed only the newer data set because the second observation is much deeper than the first. In the spectral fits, all four spectra from SIS and GIS were fitted simultaneously since the photon statistics are very good. This elliptical galaxy has a very bright extended X-ray halo with a temperature of ~ 0.8 keV. The canonical model consisting of soft thermal emission and a hard component was not acceptable because the single-temperature RS model poorly fits the low-energy portion of the spectrum. This is probably due to several complications, including the possible presence of temperature and abundance gradients, nonsolar abundance ratios, and uncertainties in the model, in particular the treatment of the Fe L emission lines. The thermal emission of this galaxy has been extensively discussed by Matsushita et al. (1997) and Matsushita, Ohashi, & Makishima (2000), and we will not address it here.

We fitted a simple power-law model to the region 4–10 keV, the latter chosen to minimize contamination from thermal emis-

sion; the best fit gives $\Gamma = 1.67^{+0.64}_{-0.60}$ and $\chi^2 = 103.7$ for 92 dof. The upper limit on the Fe K line shown in Table 10 was estimated from the same model. We tried to fit the spectrum with a thermal bremsstrahlung model instead of a power law and obtained $kT = 13.5(> 5.7) \text{ keV}$ ($\chi^2 = 103.9$, 92 dof). These results are in good agreement with the composite spectrum of elliptical galaxies given by Matsumoto et al. (1997): thermal bremsstrahlung with $kT = 12.0^{+29.3}_{-5.5} \text{ keV}$ or a power law with $\Gamma = 1.8 \pm 0.4$.

The hard-band image above 4 keV is clearly extended compared to the PSF. Therefore, the contribution of an AGN to the hard component in this galaxy is small, if any. The $L_{\text{X}}/L_{\text{H}\alpha}$ ratio calculated using the *integrated* X-ray luminosity (89) is in the range of unobscured AGNs. But the hard X-ray emission is dominated by sources other than an AGN, and the $L_{\text{X}}/L_{\text{H}\alpha}$ ratio for the *nucleus* alone should be much smaller. The X-ray output of the nucleus is probably insufficient to drive the optical line emission. The powering source of the optical emission lines and the origin of the broad H α line are thus still puzzling.

The most likely origin of the majority of the hard emission is X-ray binaries distributed over the host galaxy (see Matsushita et al. 1994). This idea has been confirmed by recent *Chandra* observations. The high-resolution image reveals an extensive population of discrete point sources, while the nucleus is not clearly detected (Loewenstein et al. 2001).

NGC 4639 (S1.0). — A detailed analysis of the *ASCA* data is presented in Ho et al. (1999). The reanalysis of the same data set in this paper shows a hint of an Fe K line. The *ROSAT* HRI image shows a pointlike nucleus (Koratkar et al. 1995). A *Chandra* image in the hard band is dominated by the nucleus.

NGC 4736 (L2). — *ASCA* and *ROSAT* results are given by Roberts, Warwick, & Ohashi (1999) and Roberts et al. (2001). They reported a marginal detection of an ionized Fe K emission line. We found a possible hint of Fe K emission in the *ASCA* spectrum, although the equivalent width in our fit is lower than previously obtained. The line center energy is consistent with a He-like ionization state for Fe, but neutral Fe cannot be ruled out. Very extended emission is seen in the *ROSAT* HRI image (Cui, Feldkhun, & Braun 1997; Halderson et al. 2001). There are several bright X-ray sources in an archival *Chandra* image of the nuclear region. The *ASCA* flux is the superposition of these sources and is not dominated by the nucleus.

NGC 4941 (S2). — The observed luminosity of this Seyfert 2 galaxy before correction of absorption is only $6.4 \times 10^{39} \text{ ergs s}^{-1}$, which is among the weakest Seyfert 2s observed thus far in the X-rays. Comparing with the results obtained with *BeppoSAX* (Maiolino et al. 1998) suggests variability of the absorption column.

NGC 5005 (L1.9). — The *ASCA* data show the presence of a pointlike hard X-ray nucleus with an X-ray luminosity consistent with that expected from the H α luminosity (Terashima et al. 2000a). Furthermore, comparison between the *ASCA* and *BeppoSAX* data (Table 15) indicates that the 2–10 keV flux has varied by a factor of 2.4 between the two observations. These characteristics strongly suggest that the nuclear source is an LLGN. A soft X-ray image taken with the *ROSAT* HRI shows an extended component ($\sim 13\%$ of the total flux; Rush & Malkan 1996) and is presumably associated with the soft

thermal plasma emission seen in our *ASCA* spectrum.

NGC 5033 (S1.5). — A detailed analysis of the *ASCA* data is presented in Terashima et al. (1999). The *ROSAT* HRI image is pointlike (Koratkar et al. 1995), as is the *Chandra* image (Ho et al. 2001).

NGC 5194 (S2). — Results of the first *ASCA* observation is presented in Terashima et al. (1998b). The second *ASCA* observation performed in 1994 is discussed in Ptak et al. (1999) and Fukazawa et al. (2001). In this paper, we concentrate on the first observation in 1993 because the SIS data in 1994 suffered from serious telemetry saturation. The hard-band image is extended and indicates that the AGN does not dominate the hard X-ray flux. The detection of a strong fluorescent Fe K line gives strong evidence for the presence of a heavily obscured AGN. Long-term variability in the hard X-ray band also supports the presence of an AGN (Table 15; see also Fukazawa et al. 2001). A recent *Chandra* spectrum that spatially isolates the nucleus confirms the presence of a strong Fe K fluorescent line (Terashima & Wilson 2001). The Compton-thick nature of the nucleus is further suggested by the *BeppoSAX* detection of an absorbed ($N_H = 5.6^{+4.0}_{-1.6} \times 10^{24} \text{ cm}^{-2}$) power-law continuum above 10 keV (Fukazawa et al. 2001).

NGC 7217 (L2). — The image in the 2–10 keV band is probably extended. A Gaussian fit to the radial surface brightness profile yielded $\sigma = 0.80 \pm 0.40$ arcmin. The flux from an AGN, even if present, thus should be lower than the observed flux. With $L_X/L_{H\alpha} = 1.2$, the observed X-ray power is insufficient to drive the optical line emission. The possibility of a Compton-thick AGN may be ruled out by the relatively low upper limit of on the EW of a fluorescent Fe K line (< 460 eV). The soft-band (0.5–2 keV) image is consistent with being pointlike ($\sigma = 0.20^{+0.19}_{-0.16}$ arcmin), but the *ROSAT* HRI image shows extended emission (Roberts et al. 2001).

NGC 7743 (S2). — This object is very faint, and we calculated the X-ray fluxes in the 0.5–2 keV and 2–10 keV band by fitting the one-dimensional projection of the SIS images along the axis connecting the nucleus with a serendipitous source located at ($23^h44^m49^s$, $09^\circ56'35''$) (J2000) on the same CCD chip. We used a width of $3/2$ to make the projected profile. This is the same technique as applied to NGC 4192 by Terashima et al.

(2000c). We estimated the spectral shape of the nucleus by using the hardness ratio (2–10 keV)/(0.5–2 keV). Assuming the Galactic absorption ($N_H = 5.3 \times 10^{20} \text{ cm}^{-2}$) and a power-law spectrum, we obtained a photon index of $1.89^{+0.16}_{-0.13}$ (errors are at 1σ). Although this value is consistent with the canonical spectrum of Seyfert galaxies, the spectral shape might be more complicated, as is the case for the other galaxies in our sample, and we cannot constrain the intrinsic absorption column density of the AGN. Using the Galactic absorption and $\Gamma = 1.9$, we derive X-ray fluxes of $4.6 \times 10^{-14} \text{ ergs s}^{-1} \text{ cm}^{-2}$ in the 0.5–2 keV band and $7.3 \times 10^{-14} \text{ ergs s}^{-1} \text{ cm}^{-2}$ in the 2–10 keV band, which correspond to X-ray luminosities of $3.3 \times 10^{39} \text{ ergs s}^{-1}$ and $5.2 \times 10^{39} \text{ ergs s}^{-1}$, respectively.

NGC 7743 is the only object in our low-luminosity Seyfert sample which does not show any signature of an AGN (see Paper II). We need future observations to see whether this object is a Compton-thick AGN or truly a Seyfert 2 nucleus without an accretion-powered source.

10. SUMMARY

We have systematically analyzed archival *ASCA* data for a large sample of LINERs and low-luminosity Seyfert galaxies in order to derive a homogeneous database of X-ray properties suitable for investigating the physical nature of low-level activity in the centers of nearby galaxies. This paper defines the sample, discusses the observations and reductions, and presents the basic quantitative measurements of the spectral, spatial, and variability properties. The next paper of this series discusses the implications of these results for a variety of issues concerning the nature of low-luminosity AGNs.

The authors are grateful to all the *ASCA* team members. Y. T. and N. I. are supported by the Japan Society for the Promotion of Science Postdoctoral Fellowships for Young Scientists. L.C.H. acknowledges financial support through NASA grants GO-06837.01-95A, AR-07527.02-96A, and AR-08361.02-97A from the Space Telescope Science Institute (operated by AURA, Inc., under NASA contract NAS5-26555). This research has made use of data obtained from the High Energy Astrophysics Science Archive Research Center (HEASARC), provided by NASA's Goddard Space Flight Center and the NASA/IPAC Extragalactic Database (NED) which is operated by the Jet Propulsion Laboratory, California Institute of Technology, under contract with NASA.

REFERENCES

- Allen, S. W., Di Matteo, T., & Fabian, A. C. 2000, *MNRAS*, 311, 493
 Awaki, H. 1999, *Adv. Space Res.*, 23 (5-6), 837
 Awaki, H., Koyama, K., Kunieda, H., Takano, S., Tawara, Y., & Ohashi, T. 1991, *ApJ*, 366, 88
 Awaki, H., Terashima, Y., Hayashida, K., & Sakano, M. 2001, *PASJ*, 53, 647
 Awaki, H., Ueno, S., Taniguchi, Y., & Weaver, K. A. 2000, *ApJ*, 542, 175
 Barth, A. J. 2002, in *Issues in Unification of AGNs*, ed. R. Maiolino, A. Marconi, & N. Nagar (San Francisco: ASP), in press
 Bassani, L., Dadina, M., Maiolino, R., Salvati, M., Risaliti, G., Della Ceca, R., Matt, G., & Zamorani, G. 1999, *ApJS*, 121, 473
 Bohlin, R. C., Savage, B. D., & Drake, J. F. 1978, *ApJ*, 224, 132
 Buote, D. A. & Fabian, A. C. 1998, *MNRAS*, 296, 977
 Burke, B. E., Mountain, R. W., Daniels, P. J., & Dolat, V. S. 1994, *IEEE Trans. NS-41*, 375
 Canosa, C. M., Worrall, D. M., Hardcastle, M. J., & Birkinshaw, M. 1999, *MNRAS*, 310, 30
 Cecil, G., Wilson, A. S., De Pree, C. 1995, *ApJ*, 440, 181
 Cui, W., Feldkuhn, D., & Braun, R. 1997, *ApJ*, 477, 693
 Dahari, O., & De Robertis, M. M. 1988, *ApJS*, 67, 249
 Dahlem, M., Weaver, K. A., & Heckman, T. M. 1998, *ApJS*, 118, 401
 Dickey, J. M., & Lockman, F. J. 1990, *ARA&A*, 28, 215
 Fabbiano, G., & Juda, J. Z. 1997, *ApJ*, 476, 666
 Falcke, H., Lehar, J., Barvainis, R., Nagar, N. M., & Wilson, A. S. 2001, in *Probing the Physics of Active Galactic Nuclei by Multiwavelength Monitoring*, ed. B. M. Peterson, R. S. Polidan, & R. W. Pogge (San Francisco: ASP), p265
 Falcke, H., Nagar, N. M., Wilson, A. S., & Ulvestad, J. S. 2000, *ApJ*, 542, 197
 Filippenko, A. V. 1996, in *The Physics of LINERs in View of Recent Observations*, ed. M. Eracleous et al. (San Francisco: ASP), 17
 Fiore, F., et al. 2001, *ApJ*, 556, 150
 Fukazawa, Y., Iyomoto, N., Kubota, A., Matsumoto, Y., & Makishima, K. 2001, *A&A*, 374, 73
 Guainazzi, M., & Antonelli, L. A. 1999, *MNRAS*, 304, L15
 Guainazzi, M., Oosterbroek, T., Antonelli, L. A., & Matt, G. 2000, *A&A*, 364, L80
 Halderson, E. L., Moran, E. C., Filippenko, A. V., & Ho, L. C. 2001, *AJ*, 122, 637
 Halpern, J. P. & Steiner, J. E. 1983, *ApJ*, 269, L37
 Heckman, T. M. 1980, *A&A*, 87, 152
 Ho, L. C. 1999, *Adv. Space Res.*, 23 (5-6), 813

- . 2002, in IAU Colloq. 184, AGN Surveys, ed. R. F. Green, E. Ye. Khachikian, & D. B. Sanders (San Francisco: ASP), in press
- Ho, L. C., et al. 2001, *ApJ*, 549, L51
- Ho, L. C., Filippenko, A. V., & Sargent, W. L. W. 1995, *ApJS*, 98, 477
- . 1997a, *ApJS*, 112, 315
- . 1997b, *ApJ*, 487, 579
- Ho, L. C., Ptak, A. F., Terashima, Y., Kunieda, H., Serlemitsos, P. J., Yaqoob, T., & Koratkar, A. P. 1999, *ApJ*, 525, 168
- Ho, L. C., & Ulvestad, J. S. 2001, *ApJS*, 133, 77
- Ishisaki, Y., et al. 1996, *PASJ*, 48, 237
- Iyomoto, N., Fukazawa, Y., Nakai, N., & Ishihara, Y. 2001, *ApJ*, 561, L69
- Iyomoto, N., & Makishima, K. 2001, *MNRAS*, 321, 767
- Iyomoto, N., Makishima, K., Fukazawa, Y., Tashiro, M., & Ishisaki, Y. 1997, *PASJ*, 49, 425
- Iyomoto, N., Makishima, K., Fukazawa, Y., Tashiro, M., Ishisaki, Y., Nakai, N., & Taniguchi, Y. 1996, *PASJ*, 48, 231
- Iyomoto, N., Makishima, K., Matsushita, K., Fukazawa, Y., Tashiro, M., & Ohashi, T. 1998, *ApJ*, 503, 168
- Kato, S., Fukue, J., & Mineshige, S. 1998, *Black-Hole Accretion Disks* (Kyoto: Kyoto Univ. Press)
- Komossa, S., Böhringer, & Huchra, J. P. 1999, *A&A*, 349, 88
- Komossa, S., & Schultz, H. 1998, *MNRAS*, 339, 345
- Koratkar, A., Deustua, S. E., Heckman, T. M., Filippenko, A. V., Ho, L. C., & Rao, M. 1995, *ApJ*, 440, 132
- Lira, P., Lawrence, A., & Johnson, R. A. 2000, *MNRAS*, 319, L17
- Loewenstein, M., Mushotzky, R. F., Angelini, L., Arnaud, K. A., & Quataert, E. 2001, *ApJ*, 552, L21
- Maiolino, R., Salvati, M., Bassani, L., Dadina, M., Della Ceca, R., Matt, G., Risaliti, G., & Zamorani, G. 1998, *A&A*, 338, 781
- Makishima, K., et al. 1994, *PASJ*, 46, L77
- . 1996, *PASJ*, 48, 171
- . 2000, *ApJ*, 535, 632
- Makishima, K., Ohashi, T., Kondo, H., Palumbo, G. G. C., & Trinchieri, G. 1990, *ApJ*, 365, 159
- Matsumoto, Y., Fukazawa, Y., Nakazawa, K., Iyomoto, N., & Makishima, K. 2001, *PASJ*, 53, 475
- Matsumoto, H., Koyama, K., Awaki, H., Tomida, H., Tsuru, T., Mushotzky, R. F., & Hastsukade, I. 1996, *PASJ*, 48, 201
- Matsumoto, H., Koyama, K., Awaki, H., Tsuru, T., Loewenstein, M., & Matsushita, K. 1997, *ApJ*, 482, 133
- Matsushita, K., et al. 1994, *ApJ*, 436, L41
- Matsushita, K., Makishima, K., Rokutanda, E., Yamasaki, N. Y., & Ohashi, T. 1997, *ApJ*, 488, L125
- Matsushita, K., Ohashi, T., & Makishima, K. 2000, *PASJ*, 52, 685
- Mitsuda, K., et al. 1984, *PASJ*, 36, 741
- Mizuno, T., Ohnishi, T., Kubota, A., Makishima, K., & Tashiro, M. 1999, *PASJ*, 51, 663
- Murphy, E. M., Lockman, F. J., Laor, A., & Elvis, M. 1996, *ApJS*, 105, 369
- Nagar, N. M., Falcke, H., Wilson, A. S., & Ho, L. C. 2000, *ApJ*, 542, 186
- Narayan, R., & Yi, I. 1994, *ApJ*, 428, L13
- Nicholson, K. L., Reichert, G. A., Mason, K. O., Puchnarewicz, E. W., Ho, L. C., Shields, J. C., & Filippenko, A. V. 1998, *MNRAS*, 300, 893
- Ohashi, T., et al. 1996, *PASJ*, 48, 157
- Pappa, A., Georgantopoulos, I., Stewart, G. C., & Zezas, A. L. 2001, *MNRAS*, 326, 995
- Pellegrini, S., Cappi, M., Bassani, L., Della Ceca, R., & Palumbo, G. G. C. 2000a, *A&A*, 360, 878
- Pellegrini, S., Cappi, M., Bassani, L., Malaguti, G., Palumbo, G. G. C., & Persic, M. 2000b, *A&A*, 353, 447
- Pérez-Olea, D. E., & Colina, L. 1996, *ApJ*, 468, 191
- Phillips, M. M., Pagel, B. E. J., Edmunds, M. G., & Díaz, A. 1984, *MNRAS*, 210, 701
- Pietsch, W., Vogler, A., Kahabka, P., Jain, A., & Klein, U. 1994, *A&A*, 284, 386
- Ptak, A. F. 1998, Ph.D. thesis, University of Maryland
- Ptak, A., Serlemitsos, P. J., Yaqoob, T., & Mushotzky, R. F. 1999, *ApJS*, 120, 179
- Ptak, A., Yaqoob, T., Mushotzky, R., Serlemitsos, P., & Griffiths, R. 1998, *ApJ*, 501, L37
- Ptak, A., Yaqoob, T., Serlemitsos, P. J., Kunieda, H., & Terashima, Y. 1996, *ApJ*, 459, 542
- Quataert, E. 2001, in *Probing the Physics of Active Galactic Nuclei by Multiwavelength Monitoring*, ed. B. M. Peterson, R. S. Polidan, & Pogge, W. San Francisco: ASP), 71
- Raymond, J. C., & Smith, B. W. 1977, *ApJS*, 35, 419
- Reynolds, C. S., Di Matteo, T., Fabian, A. C., Hwang, U., Canizares, C. R. 1996, *MNRAS*, 283, L111
- Reynolds, C. S., Nowak, M. A., & Maloney, P. R. 2000, *ApJ*, 540, 143
- Risaliti, G., Maiolino, R., & Bassani, L. 2000, *A&A*, 356, 33
- Roberts, T. P., Schurch, N. J., & Warwick, R. S. 2001, *MNRAS*, 324, 737
- Roberts, T. P., & Warwick, R. S. 2000, *MNRAS*, 315, 98
- Roberts, T. P., Warwick, R. S., & Ohashi, T. 1999, *MNRAS*, 304, 52
- Rush, B., & Malkan, M. A. 1996, *ApJ*, 456, 466
- Sambruna, R. M., Eracleous, M., & Mushotzky, R. F. 1999, *ApJ*, 526, 60
- Serlemitsos, P., Ptak, A., & Yaqoob, T. 1996, in *The Physics of LINERs in View of Recent Observations*, ed. M. Eracleous et al. (San Francisco: ASP), 70
- Serlemitsos, P. J., et al. 1995, *PASJ*, 47, 105
- Stevens, I. R., Forbes, D. A., & Norris, R. P. 1999, *MNRAS*, 306, 479
- Storchi-Bergmann, T., Baldwin, J. A., & Wilson, A. S. 1993, *ApJ*, 410, L11
- Storchi-Bergmann, T., & Pastoriza, M. G. 1989, *ApJ*, 347, 195
- Terashima, Y. 1998, Ph.D. thesis, Nagoya University
- . 1999a, *Astrophys. Let. Comm.*, 39, 149
- . 1999b, *Adv. Space Res.*, 23 (5-6), 851
- Terashima, Y., Ho, L. C., & Ptak, A. F. 2000a, *ApJ*, 539, 161
- Terashima, Y., Ho, L. C., Ptak, A. F., Mushotzky, R. F., Serlemitsos, P. J., Yaqoob, T., & Kunieda, H. 2000b, *ApJ*, 533, 729
- Terashima, Y., Ho, L. C., Ptak, A. F., Yaqoob, T., Kunieda, H., Misaki, K., & Serlemitsos, P. J. 2000c, *ApJ*, 535, L79
- Terashima, Y., Kunieda, H., & Misaki, K. 1999, *PASJ*, 51, 277
- Terashima, Y., Kunieda, H., Misaki, K., Mushotzky, R. F., Ptak, A. F., & Reichert, G. A. 1998a, *ApJ*, 503, 212
- Terashima, Y., Ptak, A. F., Fujimoto, R., Itoh, M., Kunieda, H., Makishima, K., & Serlemitsos, P. J. 1998b, *ApJ*, 496, 210
- Terashima, Y., & Wilson, A. S. 2001, *ApJ*, 560, 139
- Tully, R. B. 1988, *Nearby Galaxies Catalog* (Cambridge: Cambridge Univ. Press)
- Turner, T. J., George, I. M., Nandra, K., & Mushotzky, R. F. 1997, *ApJS*, 113, 23
- Turner, T. J., & Pounds, K. A. 1989, *MNRAS*, 240, 833
- Véron-Cetty, M.-P., & Véron, P. 1986, *A&AS*, 66, 335
- Vogler, A., Pietsch, W., & Kahabka, P. 1996, *A&A*, 305, 74
- Weaver, K. A., Wilson, A. S., Henkel, C., & Braatz, J. A. 1999, *ApJ*, 520, 130
- Whittle, M. 1992, *ApJS*, 79, 49
- Wilson, A. S., et al. 1998, *ApJ*, 505, 587
- Wilson, A. S., Yang, Y., & Cecil, G. 2001, *ApJ*, 560, 689
- Worrall, D. M., & Birkinshaw, M. 2000, *ApJ*, 530, 719
- Yamashita, A., Dotani, T., Ezuka, H., Kawasaki, M., Takahashi, K. 1999, *NIM*, A436, 68

TABLE 1
THE SAMPLE

Name	Other Name	Hubble Type	Distance (Mpc)	cz (km s ⁻¹)	Spectral Class ^a
NGC 315		E+:	65.8	4942	L1.9
NGC 404		S0-	2.4	-43	L2
NGC 1052		E4	17.8	1470	L1.9
NGC 1097		SBS3	14.5	1275	S1.5/L2
NGC 1365		SBbb	16.9	1636	S1.8
NGC 1386		SB0+	16.9	868	S2
NGC 2273		SBa:	28.4	1871	S2
NGC 2639		Sa?	42.6	3336	S1.9
NGC 2655		SAB0/a	24.4	1404	S2
NGC 3031	M81	Sab	1.4	-34	S1.5
NGC 3079		SBc spin	20.4	1125	S2
NGC 3147		Sbc	40.9	2820	S2
NGC 3507		SBb	19.8	979	L2
NGC 3607		S0:	19.9	935	L2
NGC 3998		S0?	21.6	1040	L1.9
NGC 4111		S0+:spin	17.0	807	L2
NGC 4192	M98	SABab	16.8	-142	T2
NGC 4203		SAB0-:	9.7	1086	L1.9
NGC 4258	M106	SABbc	6.8	448	S1.9
NGC 4261		E2+	35.1	2238	L2
NGC 4374	M84	E1	16.8	1060	L2
NGC 4438		S0/a:	16.8	71	L1.9
NGC 4450		Sab	16.8	1954	L1.9
NGC 4457		SAB0/a	17.4	882	L2
NGC 4501	M88	Sb	16.8	2281	S2
NGC 4565		Sb? spin	9.7	1282	S1.9
NGC 4569	M90	SABab	16.8	-235	T2
NGC 4579	M58	SABb	16.8	1519	S1.9/L1.9
NGC 4594	M104	Sa spin	20.0	1024	L2
NGC 4636		E0+	17.0	938	L1.9
NGC 4639		SABbc	16.8	1010	S1.0
NGC 4736	M94	Sab	4.3	308	L2
NGC 4941		SABab	6.4	1108	S2
NGC 5005		SABbc	21.3	946	L1.9
NGC 5033		Sc	18.7	875	S1.5
NGC 5194	M51	Sbc pec	7.7	463	S2
NGC 7217		Sab	16.0	952	L2
NGC 7743		SB0+	24.4	1710	S2

^aSpectral class of the nucleus taken from Ho et al. (1997a) except for NGC 1097 (Phillips et al. (1984); Storchi-Bergmann et al. (1993)), NGC 1365, NGC 1386 (Véron-Cetty & Véron (1986)), and NGC 4941 (Storchi-Bergmann & Pastriza (1989)), where L = LINER, S = Seyfert, T = "transition object" (LINER/H II), 1 = type 1, 2 = type 2, and a fractional number between 1 and 2 denotes various intermediate types.

TABLE 2
OBSERVATION LOG

Name	Date ^a	SIS Mode	SIS		GIS	
			count rate (counts s ⁻¹)	exposure (ks)	count rate (counts s ⁻¹)	exposure (ks)
NGC 315	1996 Aug 05	1CCD Faint	0.031	33.5	0.018	39.7
NGC 404	1997 Jul 21	1CCD Faint	—	12.3	—	13.4
	1998 Feb 06	1CCD Faint	—	27.2	—	29.7
NGC 1052	1996 Aug 11	1CCD Faint	0.046	36.5	0.041	37.7
NGC 1097	1994 Jan 12	2CCD Faint	0.079	36.7	0.055	42.0
NGC 1365	1994 Aug 12	1CCD Faint	0.019	7.9	0.024	9.5
	1995 Jan 25	4CCD Faint/Bright LD ^c 0.48 keV	0.017	35.7	0.034 ^b	39.7
NGC 1386	1995 Jan 26	4CCD Faint/Bright LD ^c 0.55 keV	0.0053	35.8	0.0063	40.1
NGC 2273	1996 Oct 20	1CCD Faint LD ^c 0.48 keV	0.004	36.1	0.013	38.4
NGC 2639	1997 Apr 16	1CCD Faint	0.008	28.3	0.005	32.1
NGC 2655	1998 Oct 29	2CCD Faint/Bright LD ^c 0.55 keV	0.012	32.6	0.009	39.6
NGC 3031	1994 Oct 21	1CCD Faint	0.35	44.0	0.19	48.3
	1995 Apr 01	1CCD Faint LD ^c 0.41 keV	0.50	18.1	0.28	21.4
	1995 Oct 24	1CCD Faint LD ^c 0.41 keV	0.44	35.5	0.25	36.4
NGC 3079	1993 May 09	1CCD Faint/Bright	0.022	37.2	0.008	41.1
NGC 3147	1993 Sep 29	4CCD Faint/Bright	0.048	21.4	0.045	38.6
NGC 3507	1998 Nov 30	1CCD Faint	0.006	40.2	0.003	43.5
NGC 3607	1996 May 26	2CCD Faint/Bright	0.011	68.5	0.007	64.5
NGC 3998	1994 May 10	2CCD/1CCD Faint	0.29	24.3	0.18	39.7
NGC 4111	1997 Dec 07	1CCD Faint LD ^c 0.48 keV	0.008	14.4	0.004	15.6
	1997 Dec 15	1CCD Faint LD ^c 0.48 keV	0.008	19.0	0.003	21.2
NGC 4192	1997 Dec 17	2CCD Faint/Bright	—	3.9	—	4.3
	1997 Dec 23	2CCD Faint/Bright	—	13.3	—	14.3
NGC 4203	1993 Dec 17	2CCD Faint	0.035	35.1	0.024	38.1
NGC 4258	1993 May 15	4CCD Faint/Bright	0.075	36.5	0.088	40.1
	1996 May 23	1CCD Faint	0.16	24.2	0.12	31.5
	1996 Jun 05	1CCD Faint	0.17	29.1	0.13	33.5
	1996 Dec 18	1CCD Faint	0.16	28.4	0.13	30.4
NGC 4261	1996 Jun 23	1CCD Faint	0.039	57.6	0.026	61.3
NGC 4374	1993 Jul 04	2CCD Faint/Bright	0.075	37.4	0.025	21.7
NGC 4438	1995 Dec 24	2CCD/1CCD Faint	0.012	21.5	0.004	20.6
	1996 Jan 05	1CCD Faint/Bright	0.014	21.6	0.004	22.6
NGC 4450	1995 Jun 20	1CCD Faint LD ^c 0.41 keV	0.026	37.4	0.015	36.7
NGC 4457	1998 Jun 14	1CCD Faint	0.01	42.1	0.005	44.0
NGC 4501	1997 Jun 22	2CCD Faint LD ^c 0.55 keV	0.019	35.7	0.013	35.4
NGC 4565	1994 May 28	2CCD Faint	0.056 ^b	37.4	0.036 ^b	38.8
NGC 4569	1997 Jun 24	1CCD Faint	0.03	21.9	0.006	21.0
	1997 Jul 06	1CCD Faint	0.03	19.0	0.007	20.4
NGC 4579	1995 Jun 25	2CCD Faint/Bright	0.15	32.0	0.090	30.9
	1998 Dec 18	1CCD Faint	0.14	18.6	0.14	19.6
	1998 Dec 28	1CCD Faint	0.14	17.6	0.12	19.4
NGC 4594	1994 Jan 20	2CCD Faint LD ^c 120 ADU	0.075	18.7	0.060	19.7
NGC 4636	1995 Dec 28	1CCD Faint LD ^c 0.48 keV	0.22	253.6	0.083	187.5
NGC 4639	1997 Dec 17	1CCD Faint	0.029	31.6	0.019	33.1
	1997 Dec 23	1CCD Faint	0.030	35.2	0.018	38.0
NGC 4736	1995 May 25	1CCD Faint LD ^c 0.41 keV	0.073	28.4	0.042	31.2
NGC 4941	1996 Jul 19	1CCD Faint	0.010	18.2	0.009	17.9
	1997 Jan 08	1CCD Faint	0.008	17.9	0.009	17.8
NGC 5005	1995 Dec 13	1CCD Faint	0.024	35.9	0.012	38.3
NGC 5033	1995 Dec 14	1CCD Faint	0.16	36.1	0.11	38.6
NGC 5194	1993 May 11	4CCD Faint/Bright	0.044	34.6	0.020	38.5
NGC 7217	1995 Nov 19	2CCD Faint/Bright LD ^c 0.48 keV	0.008	81.0	0.004	80.9
NGC 7743	1998 Dec 09	1CCD Faint	—	36.2	—	37.0

^aObservation start date.

^bCount rate includes a nearby source.

^cLevel discriminator is enabled.

TABLE 3
RESULTS OF POWER-LAW FITS

Name	N_{H} (10^{22} cm^{-2})	Γ	χ^2/dof
NGC 315	0.0	1.74	158.4/71
NGC 1052	0.0	0.20	240.8/111
NGC 1097	0.059	1.92	285.4/146
NGC 1365	0.0	2.0	276.0/180
NGC 1386	0.0	2.5	81.1/40
NGC 2273	0.0	1.25	113.4/59
NGC 2639	$0(<0.16)$	$2.1^{+0.6}_{-0.3}$	59.5/53
NGC 2655	0.0	1.1	189.8/60
NGC 3031	$0.0(<0.009)$	$1.814^{+0.016}_{-0.013}$	439.1/515
NGC 3079	0.0	2.34	134.4/90
NGC 3147	$0.062^{+0.05}_{-0.024}$	$1.82^{+0.10}_{-0.09}$	249.6/243
NGC 3507	$0(<0.072)$	$1.71^{+0.24}_{-0.22}$	27.1/25
NGC 3607	0.0	2.57	156.3/63
NGC 3998	0.082 ± 0.012	$1.90^{+0.03}_{-0.04}$	307.1/279
NGC 4111	0.0	3.1	48.7/24
NGC 4203	$0.022(<0.053)$	$1.78^{+0.07}_{-0.08}$	50.6/71
NGC 4258 (1993)	0.0	1.3	2835/172
NGC 4258 (1996)	0.0	0.22	6435/303
NGC 4261	0.0	2.3	456.4/183
NGC 4374	0.0	3.1	170.4/81
NGC 4438	0.0	2.68	58.0/42
NGC 4450	$0(<0.043)$	$1.89^{+0.14}_{-0.08}$	72.1/70
NGC 4457	0.0	2.3	50.1/27
NGC 4501	0.0	1.98	114.0/76
NGC 4552	0.0	2.35	155.7/82
NGC 4565	0.22 ± 0.04	$1.81^{+0.07}_{-0.08}$	163.7/112
NGC 4569	0.0	2.1	101.1/36
NGC 4579 (1995)	$0.043^{+0.035}_{-0.012}$	$1.80^{+0.08}_{-0.04}$	227.3/203
NGC 4579 (1998)	$0.031(<0.071)$	$1.80^{+0.06}_{-0.05}$	201/226
NGC 4594	0.056	1.61	138.7/88
NGC 4636	0.82	8.2	11495/541
NGC 4639	$0.069^{+0.041}_{-0.038}$	1.66 ± 0.10	146.4/123
NGC 4736	0.0	2.0	293.7/151
NGC 4941	0.0	0.52	134.9/55
NGC 5005	0.0	2.05	144.7/60
NGC 5033	0.087 ± 0.017	1.72 ± 0.04	173.1/186
NGC 5194	0.0	2.7	547.2/156
NGC 7217	0.0	1.77	91.5/58

TABLE 4
RESULTS OF PARTIALLY COVERED POWER-LAW FITS

Name	N_{H}^1 (10^{22} cm $^{-2}$)	N_{H}^2 (10^{22} cm $^{-2}$)	Covering Fraction	Γ	χ^2/dof
NGC 1052	0.0(< 0.034)	9.5 ± 1.6	$0.77^{+0.05}_{-0.07}$	$1.11^{+0.14}_{-0.41}$	128.6/107
NGC 2273	0.0(< 0.070)	108^{+10}_{-9}	$0.983^{+0.003}_{-0.004}$	$1.54^{+0.12}_{-0.11}$	69.1/57
NGC 2639	0.08(< 0.32)	33^{+125}_{-30}	$0.89^{+0.08}_{-0.81}$	$2.8^{+1.0}_{-0.6}$	45.8/49
NGC 2655	0.0(< 0.046)	44^{+12}_{-9}	$0.978^{+0.010}_{-0.019}$	2.6 ± 0.4	74.5/58
NGC 4565	0.30 ± 0.07	$2.9^{+0.8}_{-0.9}$	$0.65^{+0.10}_{-0.15}$	2.60 ± 0.32	140.6/110
NGC 4941	$0.16^{+0.14}_{-0.11}$	99^{+12}_{-11}	$0.966^{+0.006}_{-0.007}$	$1.48^{+0.14}_{-0.15}$	45.5 / 51

TABLE 5
RESULTS OF THERMAL BREMSSTRAHLUNG FITS

Name	N_{H} (10^{22} cm $^{-2}$)	kT (keV)	χ^2/dof
NGC 315	0.0	6.2	179.9/71
NGC 1097	0.0	5.3	418.5/147
NGC 1365	0.0	3.7	330.2/180
NGC 2655	0.0	200	193.3/60
NGC 3031	0.0(< 0.0007)	$5.16^{+0.15}_{-0.14}$	757.5/515
NGC 3079	0.0	2.1	182.7/90
NGC 3147	0(< 0.019)	$6.5^{+0.5}_{-1.2}$	256.0/243
NGC 3507	0(< 0.054)	$6.3^{+6.8}_{-2.6}$	28.7/25
NGC 3607	0.0	2.0	240.4/64
NGC 3998	0.003(< 0.010)	5.5 ± 0.3	373.8/279
NGC 4111	0.0	0.65	74.3/24
NGC 4203	0.0(< 0.005)	$6.1^{+0.9}_{-0.7}$	76.5/71
NGC 4261	0.0	2.0	619.4/183
NGC 4374	0.0	0.75	220.1 / 81
NGC 4450	0.0(< 0.009)	$3.7^{+0.8}_{-0.6}$	93.0/70
NGC 4457	0.0	3.1	70.7/27
NGC 4501	0.0	4.2	132.6/76
NGC 4552	0.0	2.1	204.8/82
NGC 4565	0.14 ± 0.03	$6.4^{+1.1}_{-0.8}$	148.2/112
NGC 4636	0.33	0.25	13008/541
NGC 4639	0.005(< 0.037)	$9.3^{+1.8}_{-2.1}$	149.0/123
NGC 4569	0.0	3.5	119.8/36
NGC 4579 (1995)	0.0(< 0.004)	$5.9^{+0.2}_{-0.7}$	260.3/203
NGC 4579 (1998)	0.0(< 0.005)	5.9 ± 0.4	232.5/226
NGC 4594	0.0 (< 0.023)	$10.2^{+2.0}_{-1.8}$	133.7/88
NGC 4636	0.26	0.32	13038/541
NGC 4639	0.005(< 0.039)	$9.3^{+2.5}_{-1.9}$	149.4/123
NGC 4736	0.0	3.1	450.4/151
NGC 5005	0.0	2.8	188.2/60
NGC 5033	0.018 ± 0.013	$7.9^{+0.8}_{-0.7}$	197.8/186
NGC 5194	0.0	0.8	748.0/156
NGC 7217	0.0	5.2	92.6/58

TABLE 6
RESULTS OF POWER-LAW + RAYMOND-SMITH MODEL FITS

Name	N_{H} (10^{22} cm^{-2})	kT (keV)	Abundances (solar units)	N_{H} (10^{22} cm^{-2})	Γ	χ^2/dof
NGC 315	0.059(f)	$0.77^{+0.05}_{-0.07}$	0.5(f) (> 0.12)	$0.49^{+0.41}_{-0.33}$	$1.73^{+0.28}_{-0.25}$	89.5/69
NGC 1052	0.030(f)	$1.0^{+2.2}_{-0.3}$	0.04(< 0.10)	$20.0^{+7.0}_{-8.3}$	$1.67^{+0.57}_{-0.40}$	104.4/104
				$2.5^{+2.7}_{-1.4}$	(CF^a $0.77^{+0.08}_{-0.10}$)	
NGC 1097	0.019(f)	$0.75^{+0.06}_{-0.12}$	0.077(> 0.040)	$0.12^{+0.21}_{-0.08}$	$1.66^{+0.13}_{-0.11}$	175.3/143
NGC 1365	0.015(f)	$0.85^{+0.05}_{-0.07}$	0.14(> 0.071)	$0.54^{+0.11}_{-0.37}$	$1.12^{+0.41}_{-0.37}$	186.7/176
NGC 1386	0.014(f)	$1.09^{+0.30}_{-0.22}$	$0.136^{+0.396}_{-0.128}$	45^{+33}_{-22}	1.7(f)	62.1/38
NGC 2639	0.027(f)	$0.81^{+0.27}_{-0.35}$	0.1(f)	0.0(< 3.1)	$1.64^{+0.91}_{-0.70}$	45.3/49
	0.027(f)	$0.80^{+0.27}_{-0.40}$	0.5(f)	0.0(< 0.31)	$1.92^{+0.18}_{-0.37}$	45.6/49
NGC 2655	0.021(f)	0.65(f)	0.1(f)	40^{+22}_{-13}	$1.2^{+0.6}_{-0.7}$	58.0/58
				0.0 (f)	(CF^a $0.91^{+0.05}_{-0.13}$)	
NGC 3031	0.042(f)	0.86(f)	0.1(f)	0.0(< 0.053)	$1.796^{+0.027}_{-0.028}$	437.4/514
	0.042(f)	0.86(f)	0.5(f)	0.0(< 0.036)	$1.803^{+0.027}_{-0.020}$	437.5/514
NGC 3079	0.008(f)	$0.33^{+0.11}_{-0.06}$	0.1(f)	0.0(< 0.09)	1.87 ± 0.18	105.1/88
	0.008(f)	$0.32^{+0.10}_{-0.06}$	0.5(f)	0.0(< 0.06)	1.93 ± 0.17	106.3/88
NGC 3507	0.016(f)	0.65(f)	0.1(f)	$1.1^{+1.0}_{-0.9}$	$2.3^{+1.0}_{-0.7}$	23.9/24
	0.016(f)	0.65(f)	0.5(f)	$0.96^{+0.85}_{-0.70}$	$2.3^{+0.9}_{-0.6}$	25.3/24
NGC 3607	0.015(f)	$0.73^{+0.06}_{-0.07}$	0.1(f)	$1.6^{+1.8}_{-1.2}$	$1.62^{+0.72}_{-0.42}$	43.1/61
	0.015(f)	$0.70^{+0.09}_{-0.06}$	0.5(f)	0.02(< 0.6)	$1.37^{+0.30}_{-0.28}$	42.8/61
NGC 4111	0.014(f)	$0.65^{+0.12}_{-0.14}$	0.1(f)	0.0(< 3.0)	$0.92^{+1.03}_{-0.62}$	14.4/22
	0.014(f)	0.66 ± 0.10	0.5(f)	0.0(< 0.47)	$1.36^{+0.46}_{-0.44}$	16.1/22
NGC 4258 (1993) ^b	0.012(f)	$0.27^{+0.02}_{-0.04}$	$0.77^{+0.05}_{-0.06}$	$0.26^{+0.03}_{-0.05}$	$12.7^{+0.9}_{-1.1}$	197.3/164
NGC 4258 (1996)	0.012(f)	0.69 ± 0.02	$0.042^{+0.007}_{-0.006}$	6.6 ± 0.3	$1.55^{+0.06}_{-0.07}$	355.6/298
NGC 4261	0.016(f)	$0.82^{+0.02}_{-0.03}$	$0.17^{+0.03}_{-0.02}$	0.17(< 0.39)	$1.30^{+0.07}_{-0.06}$	201.7/178
NGC 4374	0.026(f)	$0.78^{+0.03}_{-0.05}$	$0.12^{+0.31}_{-0.06}$	0(< 2.2)	$1.29^{+0.81}_{-0.77}$	69.1/78
NGC 4438	0.02(f)	$0.79^{+0.07}_{-0.15}$	0.1(f)	1.4(< 5.3)	$2.0^{+1.5}_{-1.0}$	35.0/40
	0.02(f)	$0.76^{+0.08}_{-0.13}$	0.5(f)	0.0(< 0.18)	$2.0^{+0.4}_{-0.3}$	34.9/40
NGC 4450	0.024(f)	$0.64^{+0.13}_{-0.31}$	0.1(f)	0.0(< 0.082)	$1.75^{+0.18}_{-0.17}$	63.9/68
	0.024(f)	$0.63^{+0.22}_{-0.32}$	0.5(f)	0.0(< 0.062)	$1.81^{+0.16}_{-0.13}$	64.2/68
NGC 4457	0.018(f)	$0.68^{+0.12}_{-0.18}$	0.1(f)	1.1(< 3.8)	$1.7^{+1.2}_{-0.8}$	18.0/25
	0.018(f)	$0.66^{+0.10}_{-0.15}$	0.5(f)	0.15(< 1.2)	$1.5^{+0.7}_{-0.4}$	18.2/25
NGC 4501	0.011(f)	$0.79^{+0.10}_{-0.16}$	0.1(f)	0.66(< 2.3)	$1.49^{+0.74}_{-0.51}$	93.6/74
	0.011(f)	$0.77^{+0.10}_{-0.14}$	0.5(f)	0.0(< 0.90)	$1.48^{+0.53}_{-0.30}$	93.8/74
NGC 4565 ^c	0.038(f)	$1.23^{+0.95}_{-0.30}$	0.1(f)	$2.6^{+1.1}_{-1.2}$	$2.51^{+0.35}_{-0.33}$	136.5/108
				$0.37^{+0.35}_{-0.15}$	(CF^a $0.70^{+0.09}_{-0.15}$)	
	0.038(f)	$1.36^{+1.56}_{-0.37}$	0.5(f)	$2.3^{+1.0}_{-0.9}$	$2.48^{+0.31}_{-0.29}$	136.0/108
				0.24 ± 0.09	(CF^a $0.68^{+0.20}_{-0.13}$)	
NGC 4569	0.029(f)	0.66 ± 0.09	0.1(f)	$1.5^{+1.2}_{-0.8}$	$2.18^{+0.71}_{-0.66}$	54.9/32
	0.029(f)	0.67 ± 0.09	0.5(f)	$1.1^{+0.9}_{-0.8}$	$2.17^{+0.62}_{-0.64}$	55.1/32
NGC 4579 (1995)	0.031(f)	$0.90^{+0.11}_{-0.05}$	0.5(f)	0.04 ± 0.03	1.72 ± 0.05	192.4/201
NGC 4579 (1998)	0.031(f)	0.90(f)	0.5(f)	0.04 (< 0.13)	1.81 ± 0.06	200.5/225
NGC 4594	0.035(f)	$0.64^{+0.18}_{-0.15}$	$0.05^{+0.07}_{-0.02}$	$0.73^{+0.36}_{-0.33}$	1.89 ± 0.17	104.9/85
NGC 4636	0.018(f)	0.77	0.31	0.15	1.32	1398.8/538
NGC 4736	0.011(f)	$0.61^{+0.05}_{-0.10}$	$0.08^{+0.50}_{-0.06}$	0.0(< 1.3)	$1.56^{+0.12}_{-0.15}$	165.3/146
NGC 5005	0.011(f)	$0.76^{+0.07}_{-0.08}$	$0.06^{+0.09}_{-0.02}$	0.10(< 0.86)	0.97 ± 0.37	71.3/57
NGC 5194	0.013(f)	$0.64^{+0.03}_{-0.04}$	$0.040^{+0.012}_{-0.009}$	$2.1^{+1.2}_{-1.0}$	$1.60^{+0.49}_{-0.47}$	186.4/151
NGC 7217	0.11(f)	$0.76^{+0.10}_{-0.13}$	0.1(f)	$1.6^{+1.6}_{-1.0}$	$2.40^{+0.79}_{-0.51}$	71.2/57
	0.11(f)	$0.74^{+0.07}_{-0.13}$	0.5(f)	$0.92^{+0.74}_{-0.62}$	$2.22^{+0.54}_{-0.44}$	71.3/57

^a The power-law component is assumed to be covered partially.

^b Two-temperature Raymond-Smith model is assumed for the soft component.

^c Fitting results of the nucleus + the off-center source.

TABLE 7
RESULTS OF THERMAL BERMSSTRAHLUNG + RAYMOND-SMITH MODEL FITS^a

Name	$N_{\text{H}}(\text{galactic})$ (10^{22} cm^{-2})	kT (keV)	Abundances (solar units)	N_{H} (10^{22} cm^{-2})	kT (keV)	χ^2/dof
NGC 315	0.059(f)	$0.77^{+0.05}_{-0.07}$	0.07	0.5(f) (>0.11)	$0.29^{+0.30}_{-0.23}$	$10.4^{+22.6}_{-4.2}$ 90.9/69
NGC 1097	0.019(f)	$0.78^{+0.05}_{-0.07}$	$0.065^{+0.045}_{-0.024}$	$0.10^{+0.16}_{-0.07}$	$12.2^{+5.3}_{-3.1}$	181.3/143
NGC 1365	0.015(f)	0.85 ± 0.03	0.14 ± 0.02	$0.72^{+0.33}_{-0.27}$	> 14	186.9/176
NGC 3031	0.042(f)	0.86(f)	0.1(f)	$0.0(< 0.009)$	$7.53^{+0.46}_{-0.43}$	510.2/514
	0.042(f)	0.86(f)	0.5(f)	$0.0(< 0.009)$	$6.40^{+0.28}_{-0.27}$	564.7/514
NGC 3079	0.008(f)	$0.33^{+0.09}_{-0.05}$	0.1(f)	$0.0(< 0.06)$	$5.0^{+2.7}_{-1.4}$	109.5/88
	0.008(f)	$0.32^{+0.07}_{-0.05}$	0.5(f)	$0.0(< 0.003)$	$4.4^{+1.9}_{-1.2}$	112.8/88
NGC 3507	0.016(f)	0.65(f)	0.1(f)	$0.71(< 1.4)$	$4.1^{+4.5}_{-2.2}$	25.0/24
	0.016(f)	0.65(f)	0.5(f)	$0.0(< 1.1)$	$9.5^{+3.9}_{-7.4}$	25.9/24
NGC 3607	0.015(f)	$0.73^{+0.06}_{-0.08}$	0.1(f)	$1.3^{+1.3}_{-1.2}$	$19(> 6.0)$	43.1/61
	0.015(f)	$0.73^{+0.06}_{-0.08}$	0.5(f)	$0.0(< 0.60)$	$30(> 9.3)$	43.0/61
NGC 4111	0.014(f)	$0.65^{+0.13}_{-0.14}$	0.1(f)	$0.49(< 2.8)$	> 5.0	14.9/22
	0.014(f)	0.66 ± 0.09	0.5(f)	$0.0(< 0.43)$	> 6.5	16.4/22
NGC 4261	0.016(f)	0.82 ± 0.02	$0.17^{+0.03}_{-0.02}$	$0.13(< 0.35)$	> 44	203.1/178
NGC 4374	0.026(f)	$0.78^{+0.04}_{-0.05}$	0.12 ± 0.03	$0.0(< 1.9)$	> 7.3	69.3 / 78
NGC 4438	0.020(f)	$0.79^{+0.07}_{-0.15}$	0.1(f)	$0.98 (< 4.2)$	$6.2(> 2.0)$	35.1/40
	0.020(f)	$0.77^{+0.07}_{-0.12}$	0.5(f)	$0.0 (< 0.19)$	$4.5^{+5.1}_{-1.8}$	36.7/40
NGC 4450	0.024(f)	$0.67^{+0.20}_{-0.27}$	0.1(f)	$0.0 (< 0.047)$	$7.2^{+1.2}_{-2.3}$	68.6/68
	0.024(f)	$0.64^{+0.18}_{-0.34}$	0.5(f)	$0.0 (< 0.026)$	$5.6^{+2.4}_{-1.4}$	72.2/68
NGC 4457	0.018(f)	$0.68^{+0.12}_{-0.16}$	0.1(f)	$0.84(< 3.1)$	$11 (> 2.8)$	17.9/25
	0.018(f)	$0.66^{+0.10}_{-0.14}$	0.5(f)	$0.07(< 0.83)$	$19 (> 4.3)$	18.1/25
NGC 4501	0.011(f)	$0.75^{+0.14}_{-0.12}$	0.1(f)	$0.37 (< 1.7)$	$34(> 5.2)$	94.0/74
	0.011(f)	$0.78^{+0.13}_{-0.13}$	0.5(f)	$0.0 (< 0.53)$	$19(> 6.7)$	94.2/74
NGC 4569	0.029(f)	$0.66^{+0.09}_{-0.12}$	0.1(f)	1.1 ± 0.8	$5.7^{+2.3}_{-2.4}$	56.2/32
	0.029(f)	$0.66^{+0.08}_{-0.20}$	0.5(f)	$0.62^{+0.67}_{-0.59}$	$6.0^{+4.1}_{-2.9}$	56.5/32
NGC 4579 (1995)	0.031(f)	$0.89^{+0.12}_{-0.04}$	0.5(f)	$0(< 0.010)$	$7.9^{+1.2}_{-0.9}$	200.3/201
NGC 4579 (1998)	0.031(f)	0.89 (f)	0.5(f)	$0.0 (< 0.082)$	$6.8^{+0.6}_{-1.0}$	213.6/225
NGC 4594	0.035(f)	$0.62^{+0.09}_{-0.21}$	$0.053(> 0.026)$	$0.42^{+0.30}_{-0.37}$	$7.5^{+3.1}_{-1.8}$	104.2/85
NGC 4636	0.018(f)	0.77	0.31	0.0	10(f)	1418.1/539
NGC 4736	0.011(f)	$0.61^{+0.06}_{-0.09}$	$0.048^{+0.041}_{-0.027}$	$0.0(< 1.0)$	16^{+12}_{-6}	164.1/146
NGC 5005	0.011(f)	0.74 ± 0.08	$0.072^{+0.11}_{-0.036}$	$0.12(< 1.0)$	> 31	72.6/57
NGC 5194	0.013(f)	$0.64^{+0.03}_{-0.04}$	0.041 ± 0.009	$1.8^{+0.8}_{-0.9}$	$28(> 8.1)$	187.4/151
NGC 7217	0.11(f)	$0.74^{+0.11}_{-0.14}$	0.1(f)	$1.0^{+1.2}_{-0.7}$	$4.0^{+3.5}_{-1.6}$	70.1/57
	0.11(f)	$0.70^{+0.12}_{-0.11}$	0.5(f)	$0.46^{+0.61}_{-0.35}$	$4.5^{+3.0}_{-1.6}$	69.6/57

^aEntries followed by “(f)” indicate that the parameter is fixed.

TABLE 8
RESULTS OF POWER-LAW + VARIABLE ABUNDANCE RAYMOND-SMITH MODEL FITS^a

Name	N_H (10^{22}cm^{-2})	kT (keV)	Abundance (O,Ne,Mg,Si)	Abundance (Fe)	N_H (10^{22}cm^{-2})	Γ	χ^2/dof
NGC 315	0.059(f)	$0.77^{+0.05}_{-0.07}$	0.5(f)	0.32 (> 0.17)	$0.61^{+0.59}_{-0.42}$	$1.70^{+0.29}_{-0.27}$	88.9/68
NGC 1052	0.030(f)	$0.84^{+0.09}_{-0.14}$	0.1(f)	0.051 < 0.12	$1.9^{+3.6}_{-0.9}$ 18^{+7}_{-5} (CF ^b $0.78^{+0.06}_{-0.11}$)	$1.55^{+0.49}_{-0.41}$	104.8/104
NGC 1097	0.019(f)	0.65 ± 0.08	0.5(f)	$0.11^{+0.07}_{-0.04}$	$0.13^{+0.10}_{-0.07}$	$1.67^{+0.09}_{-0.10}$	167.6/143
NGC 1365	0.015(f)	$0.84^{+0.04}_{-0.06}$	0.5(f)	$0.31^{+1.14}_{-0.15}$	0.0 (< 1.0)	$1.08^{+0.28}_{-0.34}$	186.7/176
NGC 3079	0.008(f)	$0.62^{+0.09}_{-0.12}$	0.5(f)	$0.048^{+0.026}_{-0.019}$	$1.7^{+1.8}_{-1.2}$	$1.96^{+0.74}_{-0.71}$	88.8/87
NGC 4261	0.016(f)	$0.81^{+0.03}_{-0.02}$	0.5(f)	0.35 ± 0.04	$0.044 (< 0.18)$	$1.37^{+0.07}_{-0.06}$	205.7/178
NGC 4374	0.026(f)	$0.77^{+0.04}_{-0.06}$	0.5(f)	$0.20^{+0.18}_{-0.06}$	0.0 (< 2.6)	$1.34^{+0.61}_{-0.77}$	67.4/78
NGC 4450	0.024(f)	$0.65^{+0.18}_{-0.30}$	0.5(f)	0.09 (> 0.03)	0.0 (< 0.32)	$1.64^{+0.30}_{-0.39}$	62.8/68
NGC 4501	0.011(f)	$0.77^{+0.10}_{-0.17}$	0.5(f)	0.16 (> 0.035)	0.59 (< 3.5)	$1.43^{+0.87}_{-0.55}$	93.3/73
NGC 4565	0.038(f)	$0.80^{+1.08}_{-0.38}$	0.5(f)	0.034 (< 0.092)	$3.4^{+1.5}_{-1.2}$ $0.52^{+0.38}_{-0.30}$ (CF ^b $0.70^{+0.11}_{-0.18}$)	$2.71^{+0.43}_{-0.53}$	133.2/107
NGC 4579 (1995)	0.031(f)	$0.89^{+0.12}_{-0.08}$	0.5(f)	0.4 (> 0.12)	0.04 ± 0.03	1.72 ± 0.05	192.6/201
NGC 4594	0.035(f)	$0.62^{+0.08}_{-0.11}$	0.5(f)	$0.11^{+0.08}_{-0.03}$	0.73 ± 0.29	1.89 ± 0.16	100.2/85
NGC 4636	0.018(f)	0.76	1(f)	0.60	0.046	1.60	1315.9/538
NGC 4736	0.011(f)	$0.61^{+0.05}_{-0.08}$	0.5(f)	0.26 ± 0.04	0.0 (< 0.031)	$1.62^{+0.10}_{-0.08}$	166.6/146
NGC 5005	0.011(f)	0.72 ± 0.09	0.5(f)	$0.14^{+0.22}_{-0.06}$	0.0 (< 0.27)	$1.06^{+0.24}_{-0.18}$	73.8/57
NGC 5194	0.013(f)	$0.60^{+0.05}_{-0.04}$	$0.15^{+0.06}_{-0.06}$	$0.046^{+0.016}_{-0.012}$	$2.2^{+1.2}_{-1.3}$	$1.65^{+0.42}_{-0.47}$	177.4/150

^aEntries followed by “(f)” indicate that the parameter is fixed.

^bThe power-law component is assumed to be partially covered.

TABLE 9
SUMMARY OF Fe K EMISSION-LINE PARAMETERS

Name	Center Energy ^a (keV)	Line Width (keV)	Equivalent Width (eV)	$\Delta\chi^2$ ^b	Notes ^c
NGC 1052	6.35 ± 0.08	0(f)	180^{+80}_{-90}	12.1	5
NGC 1365	$6.59^{+0.04}_{-0.05}$	0.002 (< 0.12)	1900^{+1000}_{-800}	36.4	2
NGC 1386	$6.50^{+0.34}_{-0.16}$	0(f)	910^{+2890}_{-770}	5.7	2
NGC 2273	$6.33^{+0.05}_{-0.03}$	0(f)	1040^{+440}_{-460}	20.1	4
NGC 2639	6.4(f)	0(f)	1490^{+11110}_{-1270}	3.3	4
	6.4(f)	0(f)	3130^{+2270}_{-2000}	6.5	2
NGC 3031	$6.59^{+0.22}_{-0.13}$	0(f)	106^{+59}_{-56}	11.0	2
NGC 3147	6.49 ± 0.09	0(f)	490^{+220}_{-230}	12.9	1
NGC 3998	$6.41^{+0.12}_{-0.19}$	0(f)	85^{+81}_{-71}	3.7	1
NGC 4258 (1993)	$6.66^{+0.20}_{-0.07}$	0(f)	108^{+73}_{-64}	7.4	2 ^d
NGC 4258 (1996)	$6.31^{+0.09}_{-0.10}$	0(f)	54^{+25}_{-27}	10.6	2
NGC 4261	$6.85^{+0.08}_{-0.15}$	0(f)	550^{+300}_{-310}	8.5	2
NGC 4579 (1995)	$6.73^{+0.13}_{-0.12}$	$0.17^{+0.11}_{-0.12}$	490^{+180}_{-190}	20.0	2
NGC 4579 (1998)	6.39 ± 0.09	0.0 (< 0.16)	250^{+105}_{-95}	17.8	2
NGC 4639	$6.67^{+0.16}_{-0.23}$	0(f)	520^{+320}_{-300}	7.7	1
NGC 4736	$6.51^{+0.42}_{-0.19}$	0(f)	334^{+233}_{-239}	5.1	2
NGC 4941	$6.35^{+0.04}_{-0.10}$	0(f)	568^{+222}_{-227}	14.9	4
NGC 5033	$6.43^{+0.13}_{-0.08}$	0.08 (< 0.23)	306^{+116}_{-119}	22.5	1
NGC 5194	$6.34^{+0.04}_{-0.13}$	0(f)	910^{+350}_{-360}	17.8	2

^aLine center energy is corrected for redshift.

^bImprovement of χ^2 by adding a Gaussian component.

^cModels applied: 1 = PL model, 2 = PL + RS model, 3 = PL + variable RS model, 4 = partial covering PL model, 5 = partial covering PL + RS model.

^dSee text for details.

TABLE 10
UPPER LIMITS ON THE EQUIVALENT WIDTH OF Fe K EMISSION

Name	Fe K 6.4 keV EW (eV)	Fe K 6.7 keV EW (eV)	$\Delta\chi^2$ (6.4 keV) ^a	$\Delta\chi^2$ (6.7 keV) ^a	Notes ^b
NGC 315	< 380	325(< 1030)	0.0	0.7	2
NGC 404	c
NGC 1097	< 160	< 210	0.0	0.1	3
NGC 2655	< 270	125(< 420)	0.0	0.6	5
NGC 3079	930(< 1960)	1320 (< 2670)	2.4	2.5	2
NGC 3507	193(< 2830)	70(< 3580)	0.0	0.0	2
NGC 3607	590(< 1260)	334(< 1220)	2.1	0.4	2
NGC 4111	< 1860	< 2800	0.0	0.0	2
NGC 4192	c
NGC 4203	< 310	< 270	0.0	0.0	1
NGC 4374	< 720	610 (< 1780)	0.0	0.9	2
NGC 4438	< 1300	< 3900	0.0	1.0	2
NGC 4450	550(< 1200)	610(< 1400)	2.5	1.7	2
NGC 4457	c
NGC 4501	1200 ⁺¹¹¹⁰ ₋₁₀₇₀	910 ⁺⁹⁰⁰ ₋₈₇₀	2.9	2.6	2
NGC 4565	240(< 620)	< 350	1.7	0.1	5
NGC 4569	< 1800	< 4800	0.0	0.0	2
NGC 4594	< 150	< 260	0.0	0.0	3
NGC 4636	250(< 540)	< 120	2.7	0.0	3
NGC 5005	200(< 810)	< 510	0.9	0.0	2
NGC 7217	< 460	< 1100	0.0	0.0	2
NGC 7743	c

^a Improvement of χ^2 by adding a Gaussian component.

^b Models applied: 1 = PL model, 2 = PL + RS model, 3 = PL + variable RS model, 4 = partial covering PL model, 5 = partial covering PL + RS model.

^c Low signal-to-noise ratio.

TABLE 11
SUMMARY OF THE SPECTRAL PARAMETERS FOR THE SOFT COMPONENT

Name	Spectral Class	kT (keV)	Abundances (solar units)	Fe Abundance (solar units)	Model ^a
NGC 315	L1.9	$0.77^{+0.05}_{-0.07}$	0.5(f)	...	PL+RS
NGC 1052	L1.9	$1.0^{+2.2}_{-0.3}$	0.04(<0.10)	...	PC+RS+GA
NGC 3998	L1.9	PL+GA
NGC 4203	L1.9	PL
NGC 4438	L1.9	$0.79^{+0.07}_{-0.15}$	0.1(f)	...	PL+RS
		$0.76^{+0.08}_{-0.13}$	0.5(f)	...	PL+RS
NGC 4450	L1.9	$0.64^{+0.11}_{-0.31}$	0.1(f)	...	PL+RS
		$0.63^{+0.22}_{-0.32}$	0.5(f)	...	PL+RS
NGC 4579 (1995)	S1.9/L1.9	$0.90^{+0.11}_{-0.05}$	0.5(f)	...	PL+RS+GA
NGC 4579 (1998)	S1.9/L1.9	0.90(f)	0.5(f)	...	PL+RS+GA
NGC 4636	L1.9	0.76	1(f)	0.60	PL+RS
NGC 5005	L1.9	$0.76^{+0.07}_{-0.08}$	$0.06^{+0.09}_{-0.02}$...	PL+RS
NGC 404	L2	^b
NGC 3507	L2	0.65(f)	0.1(f)	...	PL+RS
		0.65(f)	0.5(f)	...	PL+RS
NGC 3607	L2	$0.73^{+0.06}_{-0.07}$	0.1(f)	...	PL+RS
		$0.70^{+0.09}_{-0.06}$	0.5(f)	...	PL+RS
NGC 4111	L2	$0.65^{+0.12}_{-0.14}$	0.1(f)	...	PL+RS
		0.66 ± 0.10	0.5(f)	...	PL+RS
NGC 4192	T2	^b
NGC 4261	L2	$0.82^{+0.02}_{-0.03}$	$0.17^{+0.03}_{-0.02}$...	PL+RS+GA
NGC 4374	L2	$0.78^{+0.03}_{-0.05}$	$0.12^{+0.31}_{-0.06}$...	PL+RS
NGC 4457	L2	$0.68^{+0.12}_{-0.16}$	0.1(f)	...	PL+RS
		$0.66^{+0.12}_{-0.16}$	0.5(f)	...	PL+RS
NGC 4569	T2	0.66 ± 0.09	0.1(f)	...	PL+RS
		0.67 ± 0.09	0.1(f)	...	PL+RS
NGC 4594	L2	$0.62^{+0.08}_{-0.11}$	0.5(f)	$0.11^{+0.08}_{-0.03}$	PL+vRS
NGC 4736	L2	$0.61^{+0.05}_{-0.10}$	$0.08^{+0.50}_{-0.06}$...	PL+RS+GA
NGC 7217	L2	$0.76^{+0.10}_{-0.13}$	0.1(f)	...	PL+RS
		$0.74^{+0.07}_{-0.13}$	0.5(f)	...	PL+RS
NGC 1097	S1.5/L2	0.65 ± 0.08	0.5(f)	$0.11^{+0.07}_{-0.04}$	PL+vRS
NGC 1365	S1.8	$0.85^{+0.05}_{-0.07}$	0.14 (>0.071)	...	RS+PL+GA
NGC 2639	S1.9	$0.81^{+0.27}_{-0.35}$	0.1(f)	...	RS+PL+GA
		$0.80^{+0.27}_{-0.40}$	0.5(f)	...	RS+PL+GA
NGC 3031	S1.5	0.86(f)	0.1(f)	...	RS+PL+GA
		0.86(f)	0.5(f)	...	RS+PL+GA
NGC 4258 (1993)	S1.9	$0.27^{+0.02}_{-0.04}$	$0.26^{+0.03}_{-0.05}$...	PL+RS+RS+BRE+GA
		$0.77^{+0.05}_{-0.06}$
NGC 4258 (1996)	S1.9	0.69 ± 0.02	$0.042^{+0.007}_{-0.006}$...	PL+RS+GA
NGC 4565	S1.5	$1.23^{+0.95}_{-0.30}$	0.1(f)	...	PC+RS
		$1.36^{+1.56}_{-0.37}$	0.5(f)	...	PC+RS
NGC 4639	S1.0	PL+GA
NGC 5033	S1.5	PL+GA
NGC 1386	S2	$1.09^{+0.30}_{-0.22}$	$0.136^{+0.396}_{-0.128}$...	PL+RS+GA
NGC 2273	S2	PC+GA
NGC 2655	S2	0.65(f)	0.1(f)	...	PC+RS
NGC 3079	S2	$0.62^{+0.09}_{-0.12}$	0.5(f)	$0.048^{+0.026}_{-0.019}$	PL+vRS
NGC 3147	S2	PL+GA
NGC 4501	S2	$0.79^{+0.10}_{-0.16}$	0.1(f)	...	PL+RS
		$0.77^{+0.10}_{-0.14}$	0.5(f)	...	PL+RS
NGC 4941	S2	PC+GA
NGC 5194	S2	$0.60^{+0.05}_{-0.04}$	0.15 ± 0.06	$0.046^{+0.016}_{-0.012}$	PL+vRS+GA
NGC 7743	S2	^b

^a Model: PL = power law, PC = partially covered power law, BRE = thermal bremsstrahlung, RS = Raymond-Smith, vRS = variable abundance Raymond-Smith, GA = Gaussian. The values in parentheses are the assumed abundance of the RS component.

^b Low signal-to-noise ratio.

TABLE 12
SUMMARY OF THE SPECTRAL PARAMETERS FOR THE HARD COMPONENT.

Name	Spectral Class	N_{H} (10^{22} cm^{-2})	Photon Index	Model ^a
NGC 315	L1.9	$0.49^{+0.41}_{-0.33}$	$1.73^{+0.28}_{-0.25}$	PL+RS
NGC 1052	L1.9	$2.5^{+2.7}_{-1.4}$ $20.0^{+7.0}_{-8.3}$	$1.67^{+0.57}_{-0.40}$ (CF $0.77^{+0.08}_{-0.10}$)	PC+RS+GA
NGC 3998	L1.9	0.082 ± 0.012	$1.90^{+0.03}_{-0.04}$	PL+GA
NGC 4203	L1.9	$0.022(<0.053)$	$1.78^{+0.07}_{-0.08}$	PL
NGC 4450	L1.9	$0(<0.082)$	$1.75^{+0.18}_{-0.17}$	PL+RS (0.1)
		$0(<0.062)$	$1.81^{+0.16}_{-0.13}$	PL+RS (0.5)
NGC 4579 (1995)	S1.9/L1.9	0.04 ± 0.03	1.72 ± 0.05	PL+RS+GA
NGC 4579 (1998)	S1.9/L1.9	$0.04(<0.13)$	1.81 ± 0.06	PL+RS+GA
NGC 4636	L1.9	$0.018(\text{f})$	$1.67^{+0.64}_{-0.60}$	PL ^b
NGC 5005	L1.9	$0.10(<0.86)$	0.97 ± 0.37	PL+RS
NGC 404	L2 ^c
NGC 3507	L2	$1.1^{+1.0}_{-0.9}$ $0.96^{+1.0}_{-0.9}$	$2.3^{+1.0}_{-0.7}$ $2.3^{+0.9}_{-0.6}$	PL+RS (0.1) PL+RS (0.5)
NGC 3607	L2	$1.6^{+1.8}_{-1.2}$ $0.02(<0.6)$	$1.62^{+0.72}_{-0.42}$ $1.37^{+0.30}_{-0.28}$	PL+RS (0.1) PL+RS (0.5)
NGC 4111	L2	$0(<3.0)$ $0(<0.47)$	$0.92^{+1.03}_{-0.62}$ $1.36^{+0.46}_{-0.44}$	PL+RS (0.1) PL+RS (0.5)
NGC 4192	T2	$0.027(\text{f})$	$1.70^{+0.19}_{-0.19}$	PL ^{c,d}
NGC 4261	L2	$0.17(<0.39)$	$1.30^{+0.19}_{-0.06}$	PL+RS+GA
NGC 4374	L2	$0(<2.2)$	$1.29^{+0.81}_{-0.77}$	PL+RS
NGC 4569	T2	$1.5^{+1.2}_{-0.8}$ $1.1^{+0.9}_{-0.8}$	$2.18^{+0.66}_{-0.62}$ $2.17^{+0.82}_{-0.64}$	PL+RS (0.1) PL+RS (0.5)
NGC 4594	L2	0.73 ± 0.29	1.89 ± 0.16	PL+vRS
NGC 4736	L2	$0(<1.3)$	$1.56^{+0.12}_{-0.15}$	PL+RS+GA
NGC 7217	L2	$1.6^{+1.6}_{-1.0}$ $0.92^{+0.74}_{-0.62}$	$2.40^{+0.79}_{-0.51}$ $2.22^{+0.54}_{-0.44}$	PL+RS (0.1) PL+RS (0.5)
NGC 1097	S1.5/L2	$0.13^{+0.10}_{-0.07}$	$1.67^{+0.09}_{-0.10}$	PL+vRS
NGC 1365	S1.8	$0.54(<2.0)$	$1.12^{+0.43}_{-0.37}$	PL+RS+GA
NGC 2639	S1.9	$0(<3.1)$ $0(<0.31)$	$1.64^{+0.91}_{-1.18}$ $1.92^{+0.70}_{-0.37}$	PL+RS+GA (0.1) PL+RS+GA (0.5)
NGC 3031	S1.5	$0(<0.053)$ $0(<0.036)$	$1.796^{+0.027}_{-0.028}$ $1.803^{+0.028}_{-0.020}$	PL+RS+GA (0.1) PL+RS+GA (0.5)
NGC 4258 (1993)	S1.9	$12.7^{+0.9}_{-1.1}$	$1.65^{+0.10}_{-0.16}$	PL+RS+RS+BRE+GA
NGC 4258 (1996)	S1.9	6.6 ± 0.3	$1.55^{+0.06}_{-0.07}$	PL+RS+GA
NGC 4565	S1.5	$0.37^{+0.35}_{-0.15}$ $2.6^{+1.1}_{-1.2}$ 0.24 ± 0.09 $2.3^{+1.0}_{-0.9}$	$2.51^{+0.35}_{-0.33}$ (CF $0.70^{+0.09}_{-0.15}$) $2.48^{+0.31}_{-0.29}$ (CF $0.68^{+0.20}_{-0.13}$)	PC+RS (0.1) PC+RS (0.5)
NGC 4639	S1.0	$0.069^{+0.041}_{-0.038}$	1.66 ± 0.10	PL+GA
NGC 5033	S1.5	0.087 ± 0.017	1.72 ± 0.04	PL+GA
NGC 1386	S2	45^{+33}_{-22}	$1.7(\text{f})$	PL+RS+GA
NGC 2273	S2	$0(<0.070)$ 108^{+10}_{-9}	$1.54^{+0.12}_{-0.11}$ (CF $0.983^{+0.003}_{-0.004}$)	PC+GA
NGC 2655	S2	$0.021(\text{f})$ 40^{+22}_{-13}	$1.2^{+0.6}_{-0.7}$ (CF $0.91^{+0.05}_{-0.13}$)	PC+RS (0.1)
NGC 3079	S2	$1.7^{+1.8}_{-1.2}$	$1.96^{+0.74}_{-0.71}$	PL+vRS
NGC 3147	S2	$0.062^{+0.05}_{-0.024}$	$1.82^{+0.10}_{-0.09}$	PL+GA
NGC 4501	S2	$0.66(<2.3)$ $0(<0.90)$	$1.49^{+0.74}_{-0.51}$ $1.48^{+0.33}_{-0.30}$	PL+RS (0.1) PL+RS (0.5)
NGC 4941	S2	$0.16^{+0.14}_{-0.11}$ 99^{+12}_{-11}	$1.48^{+0.14}_{-0.15}$ (CF $0.966^{+0.006}_{-0.007}$)	PC+GA
NGC 5194	S2	$2.2^{+1.2}_{-1.3}$	$1.65^{+0.42}_{-0.47}$	PL+vRS+GA
NGC 7743	S2	$0.053(\text{f})$	$1.89^{+0.16}_{-0.13}$	PL ^{c,d}

^a Model: PL = power law, PC = partially covered power law, BRE = thermal bremsstrahlung, RS = Raymond-Smith, vRS = variable abundance Raymond-Smith, GA = Gaussian. The values in parentheses are the assumed abundance of the RS component.

^b Power-law fit in the 4–10 keV band.

^c Low signal-to-noise ratio.

^d The photon index is determined from a hardness ratio assuming a power-law spectrum and Galactic absorption. Errors are at the 1σ level.

TABLE 13
SUMMARY OF X-RAY FLUXES^a

Name	Total		Power Law		Raymond-Smith	
	(observed) 0.5–2 keV	(observed) 2–10 keV	(observed) 2–10 keV	(intrinsic) 2–10 keV	(observed) 0.5–4 keV	(intrinsic) 0.5–4 keV
NGC 315	0.450	0.908	0.892	0.935	0.271	0.325
NGC 404	< 0.011	< 0.066
NGC 1052	0.349	4.78	4.72	9.94	0.316	0.344
NGC 1097	1.27	2.08	2.04	2.07	0.551	0.587
NGC 1365	0.506	1.16	1.12	1.16	0.458	0.479
NGC 1386	0.258	0.388	1.27	1.27	0.159	0.165
NGC 2273	0.0684	1.25	1.25	8.71
NGC 2639	0.167	0.323	0.323	2.14(PC) ^b
	0.157	0.190	0.182	0.182	0.089	0.097 (0.1) ^c
	0.150	0.246	0.243	0.244	0.048	0.053 (0.5)
NGC 2655	0.210	1.04	1.03	3.03	1.46	1.57 (0.1)
NGC 3031	10.1	18.3	18.3	18.4	0.271	0.306 (0.1)
NGC 3079	0.463	0.457	0.431	0.504	0.441	0.454
NGC 3147	0.792	1.64	1.64	1.67
NGC 3507	0.090	0.161	0.158	0.178	0.055	0.058 (0.1)
	0.085	0.157	0.156	0.173	0.042	0.045 (0.5)
	0.276	0.298	0.281	0.318	0.269	0.286 (0.1)
NGC 3607	0.263	0.309	0.303	0.304	0.175	0.186 (0.5)
	4.56	8.06	8.06	8.13
NGC 4111	0.206	0.260	0.252	0.252	0.173	0.181 (0.1)
	0.194	0.225	0.222	0.222	0.128	0.134 (0.5)
NGC 4192	0.057	0.112
NGC 4203	1.19	2.05	2.05	2.06
NGC 4258 (1993)	2.06	7.13	6.55	12.3	2.38	2.48
NGC 4258 (1996)	1.83	14.4	14.3	29.9	1.90	1.98
NGC 4261	0.837	1.04	0.988	1.00	0.711	0.745
NGC 4374	1.46	0.760	0.650	0.651	1.46	1.58
NGC 4438	0.402	0.278	0.243	0.276	0.400	0.426 (0.1)
	0.406	0.272	0.262	0.263	0.189	0.201 (0.5)
NGC 4450	0.444	0.658	0.654	0.655	0.0857	0.0932(0.1)
	0.443	0.646	0.644	0.646	0.0565	0.0613(0.5)
NGC 4457	0.175	0.251	0.242	0.265	0.153	0.163 (0.1)
	0.166	0.260	0.257	0.261	0.100	0.106 (0.5)
NGC 4501	0.343	0.575	0.552	0.576	0.280	0.290 (0.1)
	0.340	0.574	0.567	0.569	0.142	0.147 (0.5)
NGC 4565	0.715	1.64	1.60	2.20	0.286	0.320
NGC 4569	0.264	0.301	0.288	0.338	0.235	0.256 (0.1)
	0.250	0.302	0.296	0.332	0.198	0.218 (0.5)
NGC 4579 (1995)	2.18	4.27	4.24	4.27	0.319	0.347 (0.5)
NGC 4579 (1998)	3.01	5.86	5.84	5.86	0.174	0.189 (0.5)
NGC 4594	1.22	2.78	2.74	2.94	0.689	0.776
NGC 4636	5.43	0.768	0.479	0.482	5.51	5.82
NGC 4639	0.436	1.07	1.07	1.07
NGC 4736	1.32	1.93	1.91	1.91	0.54	0.57
NGC 4941	0.089	1.31	1.31	9.88
NGC 5005	0.426	0.730	0.701	0.706	0.353	0.366
NGC 5194	1.26	0.919	0.854	0.999	1.28	1.34
NGC 5033	2.40	5.49	5.49	5.53
NGC 7217	0.127	0.212	0.202	0.244	0.104	0.144 (0.1)
	0.121	0.215	0.211	0.234	0.074	0.102 (0.5)
NGC 7743	0.046	0.073

^aIn units of 10^{-12} ergs cm^{-2} s^{-1} .

^bPartial covering model without a Gaussian component.

^cThe values in parentheses denote the assumed abundance of the R-S component.

TABLE 14
SUMMARY OF X-RAY LUMINOSITIES^a

Name	Total		Power Law		Raymond-Smith	
	(observed) 0.5–2 keV	(observed) 2–10 keV	(observed) 2–10 keV	(intrinsic) 2–10 keV	(observed) 0.5–4 keV	(intrinsic) 0.5–4 keV
NGC 315	23.4	47.2	46.3	48.6	14.1	16.9
NGC 404	< 0.00076	< 0.0046
NGC 1052	1.33	18.2	17.9	37.8	1.20	1.31
NGC 1097	3.20	5.24	5.16	5.22	1.39	1.48
NGC 1365	1.73	3.98	3.84	3.98	1.57	1.64
NGC 1386	0.884	1.33	4.35	4.35	0.544	0.565
NGC 2273	0.662	12.1	12.1	84.3
NGC 2639	3.64	7.03	7.03	46.6 (PC) ^b
	3.42	4.14	3.96	3.96	1.94	2.11 (0.1) ^c
	3.27	5.36	5.29	5.31	1.05	1.14 (0.5)
NGC 2655	1.50	7.43	7.36	21.6	1.04	1.12 (0.1)
NGC 3031	0.238	0.430	0.430	0.433	0.0637	0.0720 (0.1)
NGC 3079	2.31	2.28	2.15	2.52	2.20	2.27
NGC 3147	1.59	32.9	32.9	33.5
NGC 3507	0.423	0.757	0.743	8.37	0.259	2.73 (0.1)
	0.400	0.739	0.733	8.14	0.198	2.12 (0.5)
NGC 3607	1.31	1.42	1.34	1.51	1.28	1.36 (0.1)
	1.24	1.47	1.44	1.44	0.832	0.884 (0.5)
NGC 3998	25.5	45.1	45.1	45.5
NGC 4111	0.714	0.902	0.874	0.874	0.600	0.628 (0.1)
	0.673	0.780	0.769	0.769	0.444	0.464 (0.5)
NGC 4192	0.19	0.38
NGC 4203	1.34	2.32	2.32	2.32
NGC 4258(1993)	1.14	3.96	3.63	6.82	1.32	1.38
NGC 4258(1996)	1.02	8.03	7.95	16.6	1.05	1.10
NGC 4261	12.3	15.5	14.6	14.8	10.5	11.0
NGC 4374	4.93	2.57	2.20	2.20	4.68	5.08
NGC 4438	1.36	0.940	0.823	0.934	1.35	1.44 (0.1)
	1.37	0.919	0.889	0.890	0.641	0.682 (0.5)
NGC 4450	1.50	2.23	2.21	2.22	0.290	0.315 (0.1)
	1.50	2.19	2.18	2.19	0.191	0.208 (0.5)
NGC 4457	0.636	0.912	0.879	0.963	0.556	0.592 (0.1)
	0.603	0.944	0.934	0.948	0.363	0.385 (0.5)
NGC 4501	1.16	1.94	1.87	1.95	0.948	0.982 (0.1)
	1.15	1.94	1.92	1.93	0.481	0.498 (0.5)
NGC 4565	0.807	1.84	1.81	2.48	0.323	0.361
NGC 4569	0.894	1.02	0.975	1.14	0.796	0.867
	0.847	1.02	1.00	1.12	0.671	0.738
NGC 4579 (1995)	7.40	14.4	14.4	14.4	1.08	1.17 (0.5)
NGC 4579 (1998)	10.2	19.8	19.8	19.8	0.589	0.640 (0.5)
NGC 4594	5.86	13.3	13.2	14.1	3.31	3.72
NGC 4636	18.8	2.66	1.66	1.67	19.1	20.2
NGC 4639	1.48	3.62	3.62	3.62
NGC 4736	0.293	0.428	0.424	0.424	0.120	0.126
NGC 4941	0.044	0.644	0.644	4.86
NGC 5005	2.32	3.97	3.82	3.84	1.92	1.99
NGC 5033	10.1	23.0	23.0	23.2
NGC 5194	0.896	0.654	0.608	0.711	0.911	0.953
NGC 7217	0.390	0.651	0.620	0.749	0.319	0.442 (0.1)
	0.372	0.660	0.648	0.719	0.227	0.313 (0.5)
NGC 7743	0.33	0.52

^aIn units of 10^{40} ergs s⁻¹.

^bPartial covering model without a Gaussian component.

^cThe values in parentheses denote the assumed abundance of the R-S component.

TABLE 15
LONG-TERM VARIABILITY

Name	Dates	Flux ^a	Instruments	References
NGC 1052	1996 Aug 11	4.78	<i>ASCA</i>	1
	2000 Jan	4.0	<i>BeppoSAX</i>	
NGC 1365	1994 Aug 12, 1995 Jan 25 ^b	1.16	<i>ASCA</i>	2
	1997 Aug	6.6	<i>BeppoSAX</i>	
NGC 1386	1995 Jan 26	0.39	<i>ASCA</i>	3
	1996 Dec 10	0.24	<i>BeppoSAX</i>	
NGC 2273	1996 Oct 20	1.25	<i>ASCA</i>	3
	1997 Feb 22	0.99 ^c	<i>BeppoSAX</i>	
NGC 3031	1993 Apr 30–1998 Oct 20 ^d	12–40	<i>ASCA</i>	4
	1998 Jun 04	38	<i>BeppoSAX</i>	
NGC 3079	1993 May 09	0.46	<i>ASCA</i>	6
	2000 May 26	0.34	<i>BeppoSAX</i>	
NGC 3998	1988 Apr 30	15	<i>Ginga</i>	7
	1994 May 10	8.06	<i>ASCA</i>	
NGC 4258	1999 Jun 29	12.0	<i>BeppoSAX</i>	8
	1993 May 15	7.13	<i>ASCA</i>	
	1996 May 23–1996 Dec 18 ^e	14.4	<i>ASCA</i>	
	1998 Dec 19–22	8.0	<i>BeppoSAX</i>	
NGC 4565	1999 May 15–20	5.8	<i>ASCA</i>	10
	1994 May 28	1.64 ^f	<i>ASCA</i>	
	...	1.8 ^c	<i>BeppoSAX</i>	
NGC 4941	1996 Jul 19, 1997 Jan 08 ^b	1.31	<i>ASCA</i>	3
	1997 Jan 22	0.66	<i>BeppoSAX</i>	
NGC 5005	1995 Dec 13	0.73	<i>ASCA</i>	11
	...	0.3	<i>BeppoSAX</i>	
NGC 5033	1984 Feb 03	4.7	<i>EXOSAT</i>	12
	1995 Dec 14	5.5	<i>ASCA</i>	
NGC 5194	1988 May 03	6.1	<i>Ginga</i>	13
	1993 May 11	0.919	<i>ASCA</i>	
	2000 Jan 18–20	0.34	<i>BeppoSAX</i>	

References. — (1) Guainazzi et al. 2001; (2) Risaliti et al. 2000; (3) Maiolino et al. 1998; (4) Iyomoto & Makishima 2001; (5) Pellegrini et al. 2000a; (6) Iyomoto et al. 2001; (7) Awaki et al. 1991; (8) Pellegrini et al. 2000b; (9) Fiore et al. 2001; (10) Reynolds et al. 2000; (11) Risaliti et al. 1999; (12) Turner & Pounds 1989; (13) Makishima et al. 1990; (14) Fukazawa et al. 2001.

^aObserved flux in the 2–10 keV band (not corrected for absorption), in units of 10^{-12} ergs s⁻¹cm⁻².

^bThe two observations were combined.

^cNo description of a nearby source in the reference.

^dSixteen observations during this period.

^eThree observations during this period.

^fIncludes the flux from a nearby source.